

Basics of Aerodynamics and Flight Mechanics

Fluid Dynamics and the Sailplane

Inviscid Incompressible Flow

Physical properties of the atmosphere

The flow of air around a sailplane in flight is determined by the laws of fluid mechanics. The state of the air is defined by a number of physical properties such as pressure, density, temperature, compressibility, kinematic viscosity, and relative humidity. Due to gravity, the properties of the atmosphere vary with altitude. Pressure, density, and temperature all decrease with altitude. Solar radiation and topography also play a role, causing considerable variation in the atmospheric properties. This effect is especially pronounced at low altitudes.

Several standard atmospheric models are used to compare aircraft data (e.g. sailplane performance measurements) at different altitudes. Table 1 and Fig. 1 summarize some data of interest from the 1964 ICAO (International Civil Aviation Organization) Standard Atmosphere [12], a commonly used standard that represents an atmosphere free from meteorological influences. Other idealized models have been defined, including the 1962 US Standard Atmosphere (identical to the 1964 ICAO model up to 65,000 ft; revised in 1976), the 1959 ARDC (U.S. Air Force) atmosphere [17], and MIL-STD-210A, which reflects the extreme ambient temperatures encountered in polar or tropical climates. The results presented in this book are based on the 1964 ICAO model [12].

It should be emphasized that these standard atmospheric models are idealizations based on empirical data

Table 1: ICAO 1964 Standard Atmosphere [12]

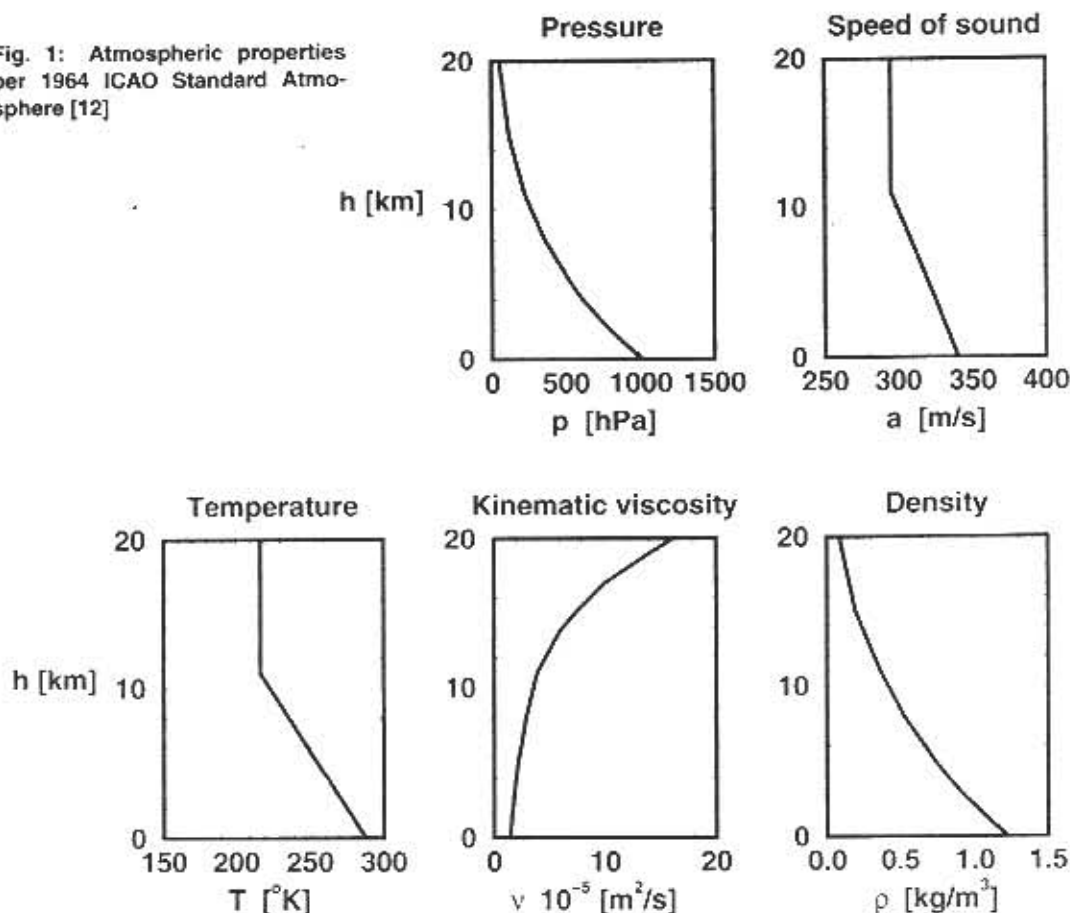
Altitude	Pressure	Density	Temp.	Kinematic Viscosity	Speed of Sound
h m	p [hPa]	ρ [kg/m ³]	T °K	ν 10 ⁻⁵ [m ² /s]	a [m/s]
0	1013.3	1.225	288.2	1.46	340.3
500	954.6	1.167	284.9	1.52	338.4
1000	898.7	1.112	281.7	1.58	336.4
1500	845.6	1.058	278.4	1.65	334.5
2000	795.0	1.007	275.2	1.71	332.5
2500	746.8	0.957	271.9	1.79	330.6
3000	701.1	0.909	268.7	1.86	328.6
4000	616.4	0.819	262.2	2.03	324.6
5000	540.2	0.736	255.7	2.21	320.5
8000	356.0	0.525	236.2	2.91	308.1
11000	226.3	0.364	216.7	3.91	295.1
15000	120.4	0.194	216.7	7.34	295.1
20000	54.7	0.088	216.7	16.15	295.1
30000	11.7	0.018	226.7	81.95	301.8

and/or simplified mathematical models. The pressure, p , density, ρ , and absolute temperature T of an ideal gas are related to one another through the *ideal gas law*,

$$p = \rho RT \quad (1)$$

where R is the specific gas constant for the gas or mixture of gases. For example, an increase in pressure results in an increase in density and/or air temperature. The process of thermal formation, familiar to all sailplane pilots, is also governed by these physical laws. Solar radiation increases the temperature near the ground, leading to a local reduction in air density. The affected parcel of air becomes buoyant and climbs skyward as a thermal.

Fig. 1: Atmospheric properties per 1964 ICAO Standard Atmosphere [12]



Often, the data in Table 1 are presented in nondimensional terms:

$$\delta = p/p_0 \quad \text{Pressure ratio} \quad (2)$$

$$\sigma = \rho/\rho_0 \quad \text{Density ratio} \quad (3)$$

$$\theta = T/T_0 \quad \text{Temperature ratio} \quad (4)$$

where p_0 , ρ_0 , and T_0 are the sea level values of pressure, density, and absolute temperature. In nondimensional units, the universal gas law (Eq. 1) becomes simply:

$$\delta = \sigma\theta \quad (5)$$

Standard atmospheric models permit the pressure and density to be expressed indirectly as altitudes. *Pressure*

altitude, (h_p) for example, is the altitude in the standard model corresponding to the ambient pressure. *Density altitude*, h_d is defined in a similar manner. Note that while h_p and h_d are expressed as altitudes [m], they actually serve to define a pressure [Pa] and density [kg/m^3].

Basics of fluid mechanics

Equation 1 is the equation of state for ideal gases at rest. The equations governing the flow about an aircraft are considerably more complicated. Air particles flowing past an aircraft are accelerated, compressed, and sheared against one another. Acceleration leads to inertial forces, com-

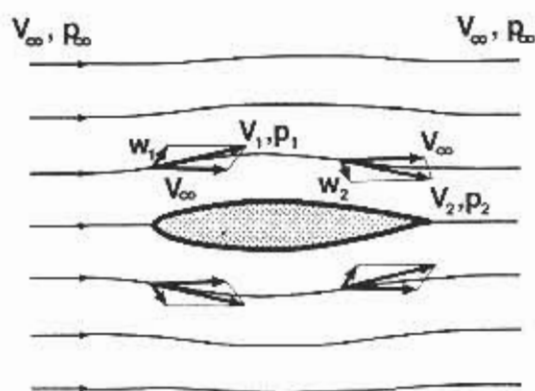


Fig. 2: Flow field near an object in steady flow.

- V_{∞} freestream velocity
- $V_{1,2}$ local velocities
- $w_{1,2}$ local perturbation velocities
- $p_{1,2}$ local pressures
- p_{∞} freestream pressure

pression to elastic forces, and shearing to viscous forces. The relationship between these forces and the geometric form of the aircraft is defined by the *Navier-Stokes equations*, the fundamental equations of fluid mechanics. Given the geometric shape of a body, for example an airfoil, the Navier-Stokes equations may be used to calculate the velocity and pressure distributions in the resulting flow.

The flow field is defined by the local velocity (speed and direction) and pressure at each point in the field. As will be discussed, the pressure and velocity at a given point are directly related to one another. The local velocity is the sum of the freestream velocity V_{∞} (the velocity of the undisturbed flow far upstream of the object) and local perturbations due to the presence of the body. The latter decrease in magnitude as the distance from the object increases (Fig. 2).

Incidentally, it does not matter whether a body is placed in a stream of flowing air — e.g. in a wind tunnel — or moves with constant velocity through a mass of still air. In both cases the flow field is identical.

The flow fields considered here are *steady*, that is, they do not vary with time. The path along which an individual air particle travels is a *streamline*. According to this definition, air particles do not move perpendicular to a streamline. Consequently, the surface of a body in a flow field must

be a streamline (two dimensional flow, for example around an airfoil section) or defined by a set of streamlines (three dimensional flow, for example a wing or fuselage). In all the cases examined here the law of conservation of mass applies — in fluid mechanics this principle is expressed through the *continuity equation*.

Reynolds number and boundary layer

Due to their complexity, the Navier-Stokes equations do not lend themselves to closed-form solutions suitable for use in calculating the aerodynamic characteristics of sailplanes. Fortunately, the nature of sailplane aerodynamics allows these equations to be simplified considerably. The primary simplification results from the fact that, throughout most of the flow field, the *inertial forces* are considerably more significant than the *viscous forces*. For a given flow field, the relationship between these forces is characterized by the *Reynolds number*, defined as follows:

$$Re = \frac{V_{\infty} l}{\nu} = \frac{\text{Inertial Forces}}{\text{Viscous Forces}} \quad (6)$$

Here V_{∞} is the freestream velocity [m/s], l a characteristic length [m] of the body (for example the airfoil chord or the fuselage length), and ν the kinematic viscosity of the air [m²/s]. The Reynolds number itself is dimensionless.

Table 2: Typical sailplane Reynolds numbers. Based on kinematic viscosity $\nu = 1.5 \cdot 10^{-5} \text{ m}^2/\text{s}$ and a range of wing chords, c.

Freestream Velocity V_{∞}	Chord c [m]	Reynolds Number Re [-]
20 m/s (72 km/h)	1.00	$1.33 \cdot 10^6$
	0.75	$1.00 \cdot 10^6$
	0.50	$0.67 \cdot 10^6$
	0.30	$0.40 \cdot 10^6$
50 m/s (180 km/h)	1.00	$3.33 \cdot 10^6$
	0.75	$2.50 \cdot 10^6$
	0.50	$1.67 \cdot 10^6$
	0.30	$1.00 \cdot 10^6$

Typical Reynolds numbers for sailplane airfoils are shown in Table 2. The data indicate that the inertial forces in the flow field about a sailplane are around a million times larger than the viscous forces. For this reason the viscous forces can be neglected throughout most of the field, allowing use of the simpler inviscid flow equations. Viscous forces become significant only in a relatively thin layer near the surface of the aircraft, the *boundary layer*. The higher the Reynolds number, the thinner the boundary layer becomes relative to the characteristic length of the body. The boundary layer near the leading edge of a sailplane wing is typically around a few millimeters thick, growing steadily to a centimeter or more near the trailing edge.

The idea of splitting the fluid flow problem into an inviscid, potential theory part and a viscous part, the boundary layer, originated with L. Prandtl in 1904 and is the cornerstone of modern fluid mechanics and aerodynamics. Boundary-layer theory plays a crucial role in determining the aerodynamic properties of an aircraft and has become a science of its own (see H. Schlichting [22]). Airfoil drag and maximum lift coefficients are strongly affected by boundary-layer phenomena. On the other hand, the effect on pressure distribution and lift is relatively insignificant. An underlying assumption in boundary-layer theory is that the static pressure at a given point on the surface of an aircraft remains constant throughout the thickness of the boundary layer. In other words: the pressure at the edge of the boundary layer is identical to the pressure at the corresponding location on the aircraft surface (Fig. 3).

$$p(x, z^*) = p(x, 0) \quad (7)$$

When determining the pressure distribution and lift (with the exception of the maximum lift) one may assume inviscid

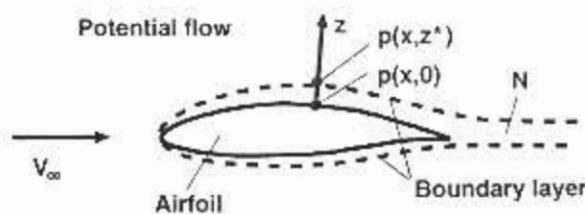


Fig. 3: Potential (inviscid) and viscous flow.

N airfoil wake
 p static pressure

cid flow without introducing significant errors. Improved results are obtained by correcting the pressure distribution to account for the thickness of the boundary layer.

The assumption of inviscid flow reduces the Navier-Stokes equations to the considerably simpler *Euler equations*. It can be shown that all solutions to the *potential equation*, a well known equation in mathematical physics (electromagnetic theory, in particular), are also solutions to the Euler equations. Inviscid flow around an airfoil or a three-dimensional body is therefore referred to as *potential flow*.

Mach number and incompressible flow

A further simplification results from the fact that sailplane airspeeds are small compared to the speed of sound ($a = 340\text{m/s}$ at sea level). The ratio of the airspeed to the speed of sound is the *Mach number*.

$$M = \frac{V_\infty}{a} = \text{Mach number} \quad (8)$$

At low Mach numbers (M less than around 0.3), the elastic forces in the air flow can be neglected, *i.e.* the air can be considered incompressible without significant error. In this case the density ρ becomes a constant, no longer dependent on the pressure. Since, for the most part, sailplanes fly with $M < 0.3$, this book assumes incompressible flow throughout.

This assumption is not warranted in the case of modern transport and military aircraft. Unlike sailplanes, these aircraft require swept wings to perform well at high subsonic Mach numbers.

Some elementary solutions to the potential equation

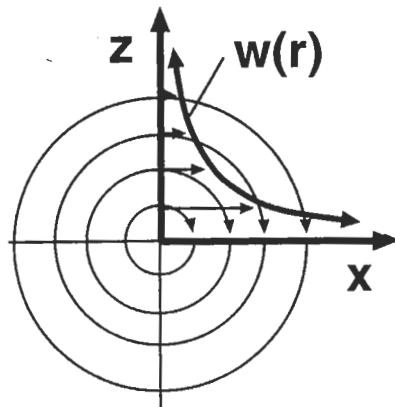
For incompressible flow, the potential equation is linear and thus particularly easy to solve. The property of linearity permits solution of complex flow fields by superimposing elementary solutions of the potential equation. Airfoil and wing theory employs *linear superposition* to build up complex solutions from the following basic solutions to the potential equation (Fig. 4):

- uniform translational flow
- point vortex
- sources and sinks

Translational flow



Potential vortex



Potential source

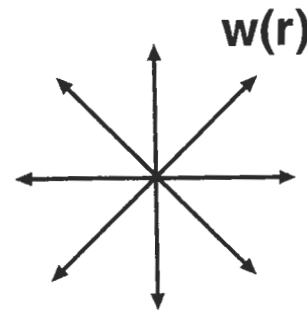
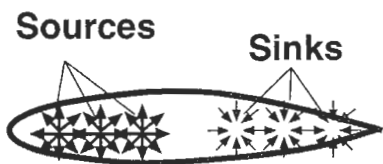
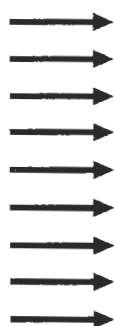
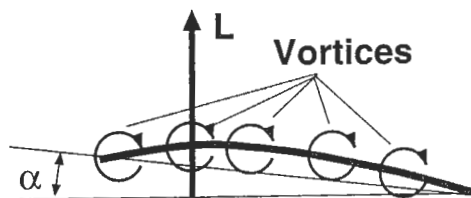
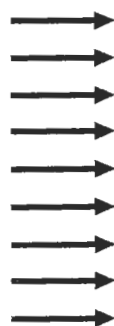


Fig. 4: Elementary solutions to the potential flow equation.

w local velocity
r distance from center



Airfoil Form



Camber Line

α Angle of attack
L Lift

Fig. 5: Thickness form and camber line formed by superposition of sources, sinks, and vortices in uniform translational flow.

For example, linear superposition can be used to calculate the flow field around a symmetric airfoil at zero angle of attack by combining the solutions of a system of sources. An airfoil at a non-zero angle of attack and/or with camber

can be formed by adding a system of point vortices (Fig. 5).

The mathematics involved in developing solutions to the potential equation need not be discussed here in great detail. However, it should be mentioned that there is a

direct relationship between vorticity and lift that plays an important role in determining the flow about a complete three-dimensional wing. This will be discussed in a following section — but first another important result must be introduced.

Bernoulli's equation

Integrating the Euler equations leads to a relationship known as *Bernoulli's equation* (Eq. 9), which states that in steady, incompressible, inviscid flow, the total pressure p_T , i.e. the sum of the static pressure p and the dynamic pressure q , remains constant along a streamline. If the flow is irrotational, the result applies to the entire flow field. This means, for example, that the sum of the static and dynamic pressures far upstream of the aircraft (p_∞ and q_∞ , respectively) is equal to the sum of the local static and dynamic pressure p_1 and q_1 at any arbitrary point on the aircraft (Fig. 6):

$$\begin{aligned} p_T &= p_\infty + q_\infty && \text{Bernoulli's Equation.} \quad (9) \\ &= p_1 + q_1 \end{aligned}$$

The dynamic pressure is a measure of the kinetic energy of the air particles in the flow field and is defined as follows:

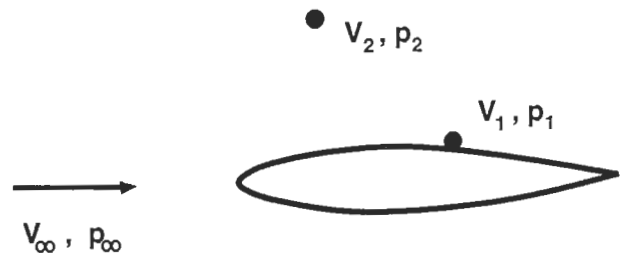
$$q_\infty = \frac{\rho}{2} V_\infty^2 \quad \text{Dynamic Pressure.} \quad (10)$$

The static pressure is a measure of the potential ("pressure") energy of the air particles. In this interpretation, Bernoulli's equation is an expression of the law of conservation of energy. An increase in the local kinetic energy (i.e. local velocity) is accompanied by a corresponding reduction in potential energy (static pressure). As will be discussed, this exchange between pressure and velocity is of particular significance to the production of lift.

Airspeed measurement

Total pressure, static pressure, and dynamic pressure can be measured using static ports and/or probes positioned within the air flow (Fig. 7).

The total pressure is measured with a *Pitot tube*, a tube with an opening on the forward end into which the freestream enters and is decelerated to zero velocity. The total pressure and static pressure measurements are often combined in a single *Prandtl tube* (Pitot-static tube, Fig. 7).



$$p_T = \frac{\rho}{2} V_\infty^2 + p_\infty = \frac{\rho}{2} V_1^2 + p_1 = \frac{\rho}{2} V_2^2 + p_2$$

Fig. 6: Relationship between velocity and static pressure (Bernoulli's equation)

Instead of a combined Pitot-static tube, a simple Pitot tube may be used together with static ports positioned at points on the aircraft surface where the local static pressure is approximately equal to the freestream static pressure. However, the ideal position varies with angle of attack (i.e. airspeed), giving rise to a *position error* in the airspeed measurement. Static pressure may also be measured using a simple tube, closed at the front, with holes drilled on its sides some distance from the forward end.

Dynamic pressure is the difference between the measured freestream static pressure p and total (Pitot) pressure p_T . The airspeed indicator is essentially a pressure gauge that measures the difference between the static and total pressure. From Eqs. 9 and 10:

$$V_\infty = V_{TAS} = \sqrt{(2/\rho)(p_T - p)} \quad (11)$$

Since the air density ρ varies with ambient conditions (in particular, altitude), the airspeed indicator is calibrated to sea level standard conditions:

$$V_{EAS} = \sqrt{(2/\rho_0)(p_T - p)} \quad (12)$$

V_{EAS} , the *equivalent airspeed*, is equal to the true airspeed only at sea level standard conditions. V_{EAS} is the primary quantity of interest when considering the forces acting on a sailplane. In JAR-22 [49] the airspeeds at which the maneuver loads, gust loads, and flutter characteristics must be investigated are equivalent airspeeds, V_{EAS} .

A simple relationship between equivalent and true airspeeds can be derived from Eq. 3 and the definition of dynamic pressure, q_∞ (Eq. 10):

$$V_{EAS} = \sqrt{\sigma} V_{TAS} \quad (13)$$

Fig. 7: Pressure measurement for airspeed systems

- (a) Pitot probe (total pressure)
- (b) Static probe (static pressure)
- (c) Pitot-static (Prandtl) tube (dynamic pressure)

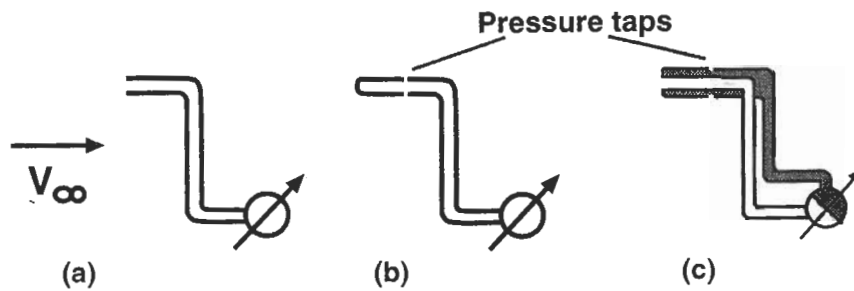
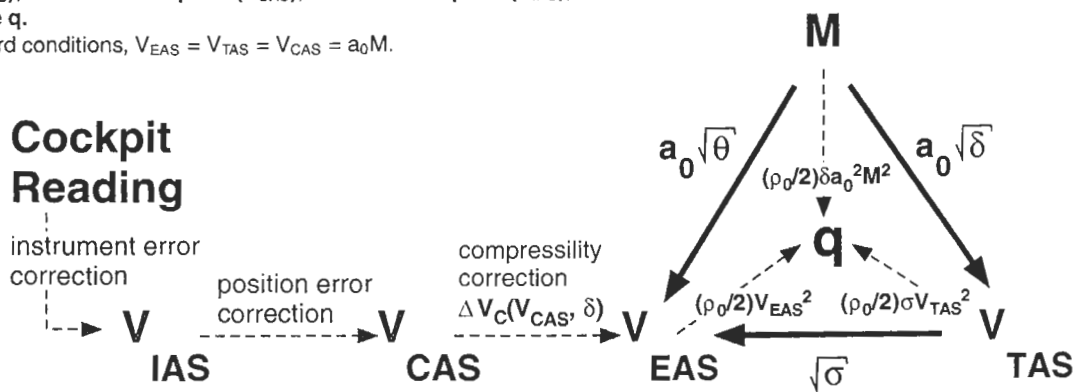


Fig. 8: Relationship between Mach number (M), equivalent airspeed (V_{EAS}), true airspeed (V_{TAS}), calibrated airspeed (V_{CAS}), indicated airspeed (V_{IAS}), and dynamic pressure q .

In sea level standard conditions, $V_{EAS} = V_{TAS} = V_{CAS} = a_0 M$.



Both equivalent and true airspeed are directly related to Mach number. The speed of sound in dry air varies only with ambient temperature:

$$a = \sqrt{\gamma RT} \quad (14)$$

where γ is the *specific heat ratio* ($\gamma = 1.4$ in air). This relationship, together with the definition of Mach number (Eq. 8), the universal gas law (Eq. 5), and Eq. 13, lead to the following simple relationships:

$$V_{EAS} = a_0 M \sqrt{\delta} \quad (15)$$

$$V_{TAS} = a_0 M \sqrt{\theta} \quad (16)$$

The relationship between true airspeed, equivalent airspeed, Mach number, and dynamic pressure is shown schematically in Fig. 8.

Due to the effects of compressibility, the total pressure in the Pitot tube is slightly higher than that predicted by

Bernoulli's equation. Thus, even assuming zero static position error and a perfectly calibrated instrument, the airspeed indicator may indicate an airspeed that is slightly higher than V_{EAS} . This is the *calibrated airspeed*, V_{CAS} . Since the compressibility correction varies with pressure ratio, δ , it is not possible to calibrate an airspeed indicator to indicate equivalent airspeed at all altitudes. In practice, airspeed indicators are calibrated so that compressibility correction ΔV_C is zero at sea level (*i.e.* $V_{CAS} = V_{EAS}$). Sailplanes typically operate at airspeeds and altitudes for which the compressibility correction is negligible — at $h_p = 10,000$ m and $V_{CAS} = 300$ km/h, the correction ΔV_C is only approximately 3 km/h. The details of the calculation of the compressibility correction may be found in texts on aircraft performance, for example S. K. Ojha [19].

Another parameter of interest is the *indicated airspeed*, V_{IAS} . This is what the pilot reads on the airspeed indicator, and reflects all sources of error (compressibility, po-

sition error, instrument calibration, etc.). Unlike the structural requirements, which are defined with respect to equivalent airspeeds, JAR-22 requires that operating airspeed limitations be provided to the pilot in terms of *indicated* airspeed [49].

In this book, where not otherwise specified, airspeeds are assumed to be V_{TAS} .

Lift and Potential Flow

Circulation and lift

The primary purpose of the wing is to provide lift. Central to the production of lift is the relationship between the wing geometry (airfoil, planform, and twist) and the distribution of lift over its surface. This relationship is calculated using point vortices and a derived quantity, *circulation*.

An individual vortex is associated with a radially symmetric velocity field having circular streamlines centered around the vortex location (Fig. 9). The velocity w is constant along a given streamline, but decreases with the distance from the vortex center. Multiplying the velocity w at a distance r with the length of the streamline (that is, the circumference of a circle with radius r) yields the circulation:

$$\Gamma = 2\pi r w(r) \quad (17)$$

The flow about a vortex has the property that the circulation measured along any path enclosing the vortex is the

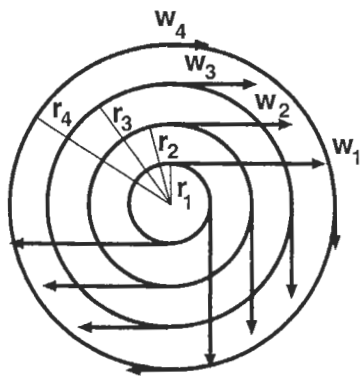


Fig. 9: Velocity field induced by a two-dimensional vortex of strength Γ .

$$\Gamma = 2\pi r_1 w_1 = 2\pi r_2 w_2 = 2\pi r_3 w_3 = 2\pi r_4 w_4$$

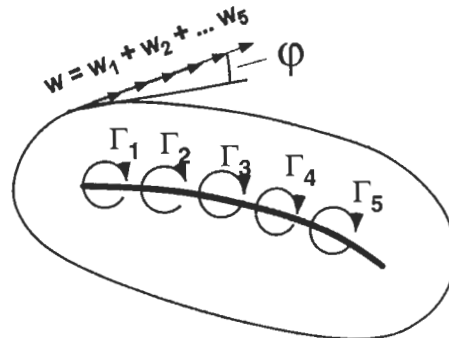


Fig. 10: Circulation around a system of two-dimensional vortices. $\Gamma = \Gamma_1 + \Gamma_2 + \Gamma_3 + \Gamma_4 + \Gamma_5$

same, regardless of the shape or size of the path. This result is generalized to a system of vortices: the circulation measured about any closed path enclosing a system of vortices is equal to the sum of the circulation due to each individual vortex (Fig. 10):

$$\Gamma = \oint w \cos \phi ds \quad (18)$$

$$\Gamma = \Gamma_1 + \Gamma_2 + \Gamma_3 + \Gamma_4 + \Gamma_5$$

Fig. 11 shows the velocity field due to a system of vortices superimposed on a uniform translational flow field. Above

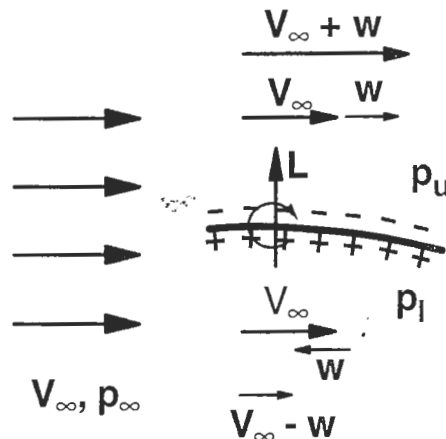


Fig. 11: Lift produced by superposition of a system of vortices in uniform translational flow.

w perturbation velocity induced by vortex system

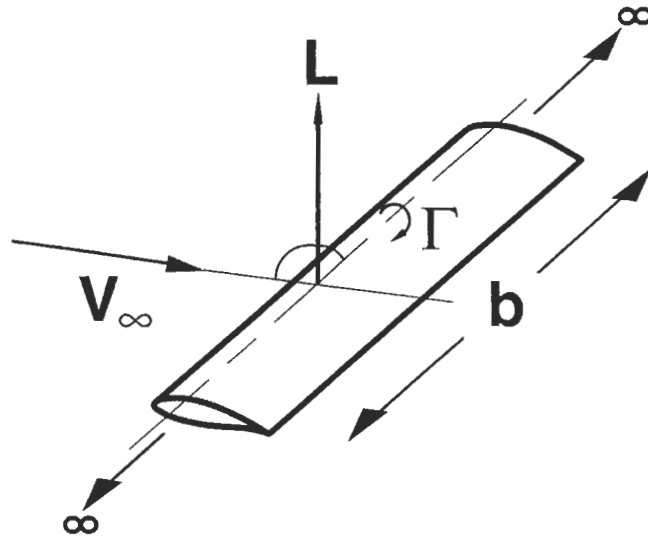
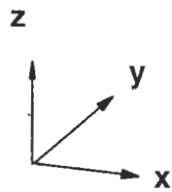


Fig. 12: Lift L due to bound vortex of strength Γ in potential flow. According to the Kutta-Joukowski theorem, lift $L = \rho V \Gamma b$ and is perpendicular to both velocity vector and bound vortex.

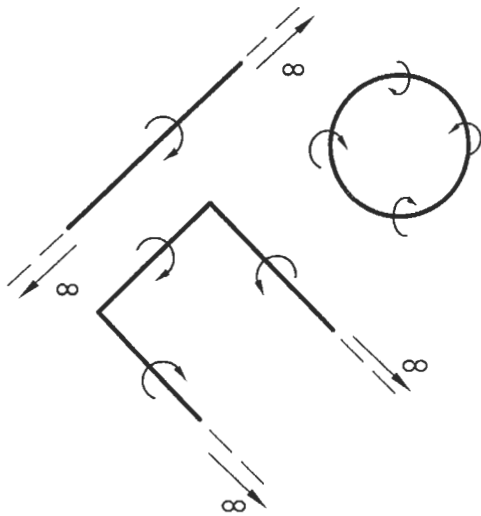


Fig. 13: Vortex models in Helmholtz vortex theorem.

- infinitely long vortex
- ring vortex
- horseshoe vortex

the vortex system, the translational velocity V_∞ is added to the velocity due the vortex system, resulting in an increased velocity $V_\infty + w$. On the other hand, below the vortex

system the velocity contribution from the vortices opposes the freestream velocity, resulting in a reduced total velocity of $V_\infty - w$. Therefore, according to Bernoulli's equation, the static pressure above the vortex system p_u is lower than the freestream pressure, p_∞ , and below the vortex system the static pressure p_l is higher. If the vortex system is located within an airfoil, this pressure difference results in an upwards force L perpendicular to the freestream velocity V_∞ . By convention, the force acting perpendicular to the direction of flow is defined as lift, and the force along the direction of flow, drag.

The lift L is proportional to the total circulation Γ of the vortex system, the freestream velocity V_∞ , the density ρ , and the span b (Fig. 12):

$$L = b\rho V_\infty \Gamma \tag{19}$$

This result is the *Kutta-Joukowski* theorem.

Modeling wings with vortices

Before the Kutta-Joukowski theorem is used to calculate the flow about a wing, a few special characteristics of vortices must be mentioned. According to the *Helmholtz vortex theorem* individual vortices in an inviscid three-dimensional flow field neither begin nor end in the fluid — they must either be infinitely long or form a closed path (Fig. 13). This property leads to a distinction between the

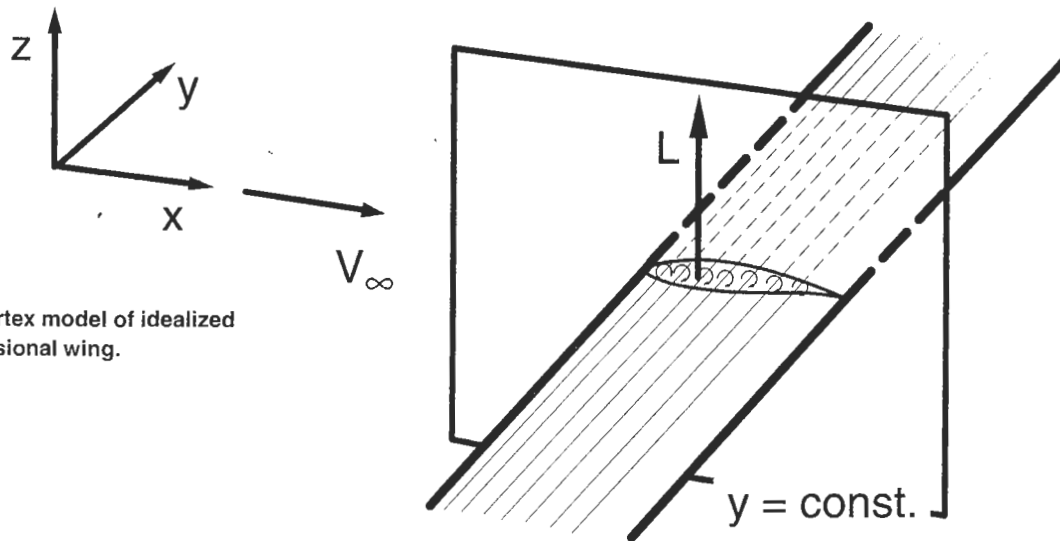


Fig. 14: Vortex model of idealized two-dimensional wing.

two-dimensional problem (airfoil theory) and the three dimensional problem (wing theory).

For a two-dimensional wing, the vortex model consists of a system of infinitely long vortex filaments distributed along the chord of the wing (Fig. 14). The two dimensional wing extends to infinity in the y -direction — that is, perpendicular to the freestream velocity and direction of lift. The flow field is thus identical in any plane defined by $y=\text{constant}$. Airfoil geometry and pressure distribution are functions of x and z only, hence the term “two-dimensional” wing.

The vortex model for a finite span wing is considerably more complicated. According to the Helmholtz vortex theorem, the vortex filaments cannot simply come to an end at the wingtips, but instead bend backwards, extending downstream to infinity. This forms a *horseshoe vortex*, consisting of a “bound” vortex within the wing and a pair of free vortices trailing aft from the wing tips (Fig. 15).

If a wing were modeled with a single horseshoe vortex, the lift would be evenly distributed along its span. In reality, the lift (in other words, the circulation) varies along the wing, tapering to zero at the tips. At a given point on the wing, a spanwise change in the bound circulation $\Delta\Gamma$ must be accompanied by a trailing vortex of the same strength. One can thus model the flow about a wing with a system of superimposed horseshoe vortices (Fig. 16). The trailing vortices are particularly strong near the tip, tending to “roll up” a short distance downstream of the wing to form a

pronounced tip vortex. Tip vortices are easily visualized, for example, with a small windmill placed downstream of the wingtip of a wind-tunnel model.

Just as the lift on a wing can be determined by combining a system of vortices with a uniform flow field, the actual form of the aircraft, in particular the thickness distributions of the wing and fuselage, can be modeled by further superimposition of a system of sources. This need not be discussed in detail here; rather, the reader is referred to the aerodynamics texts listed at the end of this section.

Velocity induced by a vortex system

Uniform translational flow is characterized by constant velocity and pressure. Introducing a system of sources, sinks, and vortices produces an additional velocity field, inducing a perturbation velocity throughout the entire flow field. The local velocity at a given point in the field is the sum of the translational and perturbation velocities, with the local static pressure following from Bernoulli's equation.

Induced effects are of particular importance to aircraft design and analysis. For example, an analysis of the flow around a wing must consider the fact that the wing is operating in an induced flow field generated by its own vorticity. The fuselage and empennage are also affected by the velocity field induced by the wing, and in turn gener-

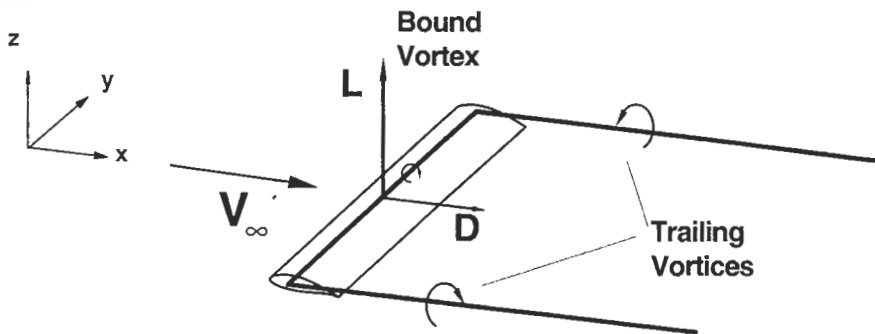


Fig. 15: Three-dimensional wing modeled with simple horseshoe vortex.

L Lift
D Drag

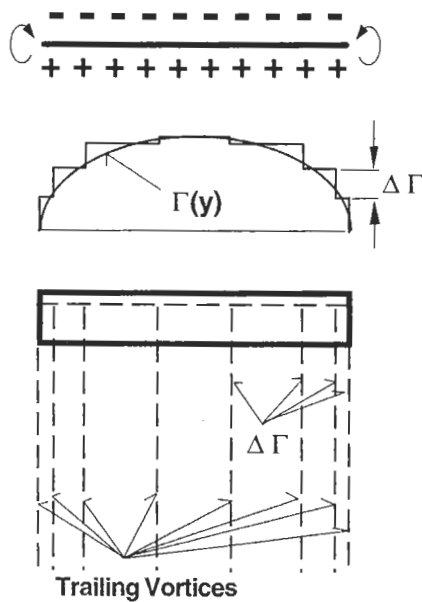


Fig. 16: Representation of a three-dimensional wing by a system of horseshoe vortices.

- pressure equalization at wingtips
- circulation distribution
- vortex system

ate an induced flow field affecting the wing. These latter effects are termed *wing-fuselage interference* and *wing-empennage interference*. The wing induces an upwash on the portion of the fuselage extending upstream of the wing, and a downwash on the aft portion of the fuselage and

empennage. This variation in induced velocity along the longitudinal axis of the sailplane influences the design of the fuselage and horizontal stabilizer (Fig. 17).

The velocity field associated with a system of vortices and potential sources is calculated using the *Biot-Savart law*. For the general case of a vortex system of arbitrary geometry, the resulting expressions can be quite complex. Considerable simplification results, however, by assuming that the vortex filaments are straight and infinitely long. Fortunately, in the case of sailplane wings, this proves to be a valid assumption.

Computational methods in wing and airfoil aerodynamics

Analytic methods for wing and airfoil aerodynamics are directed at two problems. In the first, a pressure and velocity distribution over the airfoil and/or wing are specified, and the airfoil and wing planform required to generate these distributions are determined. This is the *design problem* (also called the *inverse problem*). In the second case, the airfoil and wing planform are prescribed, and the resulting pressure and velocity distributions are computed. This task is the *analysis problem*. Both problems arise frequently in the course of aircraft design.

Computational methods for sailplane aerodynamics are based on the vortex and potential source models described in the previous sections. Another class of methods, based on *conformal mapping*, are frequently used as well. Practical implementations of computational methods have been developed by Riegels, Weber, Eppler and Drela [1, 23, 24, 173, 177-180, 191].

Typically, the problem is broken down into two parts. (1)

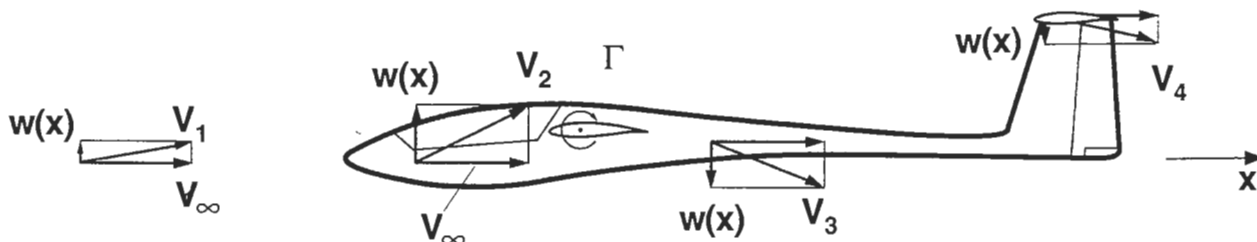


Fig. 17: Velocity perturbations induced by wing on fuselage and empennage

determination of the induced velocity over the wing using the Biot-Savart law and (2) application of a kinematic boundary condition to obtain the actual flow field about the wing. The boundary condition states that at every point on the wing the resultant velocity is parallel to the local surface (Fig. 18). This is equivalent to stating that no air flows through the surface of the wing.

The mathematical expression of the kinematic boundary condition can be quite complex and, depending on the method used, finding a solution to the governing equations that satisfies the boundary conditions can require considerable computational effort.

While the most powerful computational hardware is usually found at universities and research organizations, the advent of inexpensive personal computers has made it possible for almost anyone to make use of sophisticated computational tools for aerodynamic analysis. Several software packages are commercially available. A detailed understanding of the underlying theory is not absolutely necessary; it suffices to understand the preparation of the input data such as airfoil coordinates, analysis options, and so forth.

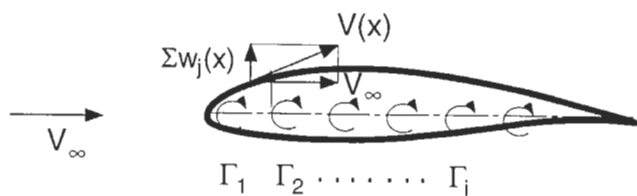


Fig. 18: Kinematic boundary condition. Local velocity is tangent to airfoil surface.

One important boundary condition is the *Kutta condition*, which plays a central role in determining the flow about an airfoil. The Kutta condition states that the flow departs the sharp trailing edge of an airfoil in a smooth fashion, or, said another way, that the rear stagnation point always lies at the airfoil trailing edge¹. The Kutta condition establishes the circulation about an airfoil, and for this reason small modifications to the trailing edge can have a significant effect on its lift.

The aerodynamics of a finite span wing depend on the effects of the vorticity it trails downstream. Analyzing a wing of arbitrary planform requires considerable computational effort because the effects of the complete vortex system must be integrated over the entire wing. The well known *lifting-line theory* of L. Prandtl, the first method to allow calculation of the aerodynamic characteristics of a finite-span wing, is based on a number of simplifying assumptions (Fig. 19):

- The wing and its system of trailing vortices lie entirely in the $x - y$ plane.
- The wing is unswept and the trailing vortices are consequently of equal length.
- At any spanwise location y , the local downwash induced by the trailing vortex system does not vary over the chord of the wing.

The latter assumption implies that the wing chord is small compared to the wing span, *i.e.* the aspect ratio is large (a value of $\mathcal{R} = 5$ is considered the minimum for application

¹for cusped trailing edges, the condition simply requires the upper and lower surface velocities to be identical at the trailing edge

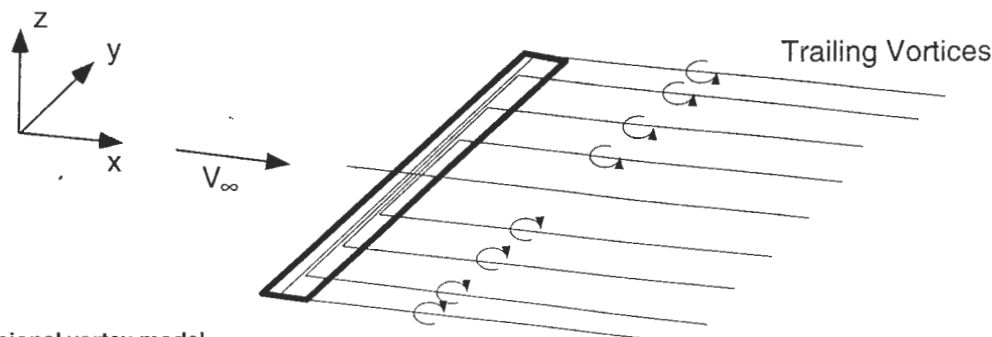
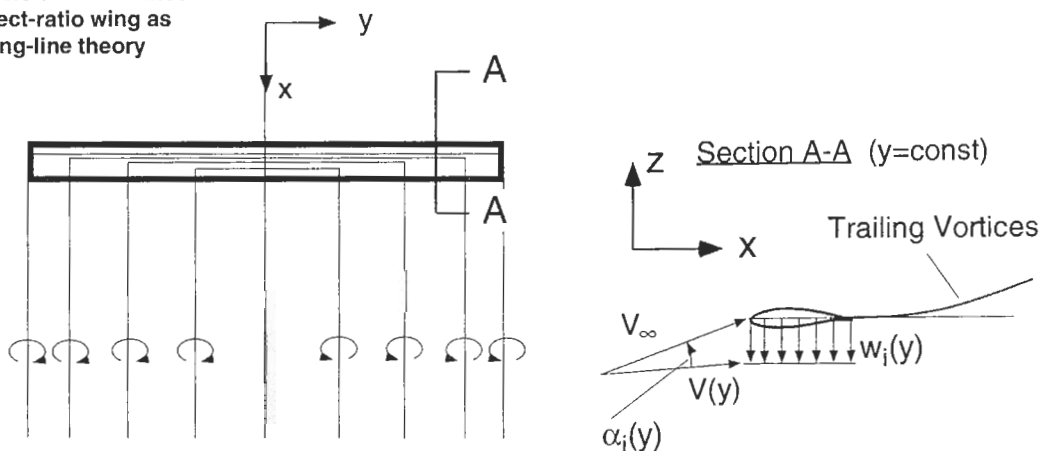


Fig. 19: Three-dimensional vortex model of unswept high aspect-ratio wing as used in Prandtl's lifting-line theory



of lifting-line theory), and allows the downwash w_i to be treated as a function of a single variable, the spanwise coordinate y .

The effect of superimposing the induced downwash w_i on the free stream velocity V_∞ can be approximated by rotating the free stream velocity V_∞ through an angle $\tan \alpha_i(y) = w_i(y)/V_\infty$. As with the downwash, this *induced angle of attack* varies along the wing span.

The wing has a geometric angle of attack α_g relative to the direction of flight, *i.e.* to the free stream velocity V_∞ far upstream of the sailplane. If the wing is built with twist, the geometric angle of attack will vary along the span of the wing, and is therefore a function of the spanwise coordinate y as well.

The induced downwash has the effect of reducing the geometric angle of attack at a given spanwise location by an amount equal to the induced angle of attack, resulting

in an effective angle of attack (Fig. 20):

$$\alpha_e(y) = \alpha_g(y) - \alpha_i(y) \quad (20)$$

This is an equation of considerable importance. It may be interpreted as follows: At each location along the span of an unswept, high aspect ratio wing subject to a steady free stream velocity at angle of attack α_g , the local aerodynamics may be represented by a two-dimensional section having an identical airfoil and operating at an effective angle of attack α_e .

This result allows the results of two-dimensional airfoil theory to be transferred to a finite span wing on a section-by-section basis. The pressure distribution over a cross section of a three-dimensional wing can therefore be determined from two dimensional results obtained for the same airfoil operating at the effective angle of attack, α_e .

Incidentally, for a given lift (that is, for a sailplane of given

weight), the greater the wing span, the smaller the downwash and induced angle of attack. As the span increases without limit, the downwash approaches zero and the flow about the wing becomes increasingly two-dimensional.

Prandtl's lifting-line theory allows us to calculate the induced angle of attack and sectional (local) lift along the wing span. However, despite the simplified vortex system that assumed by the theory, the mathematics remain somewhat complex (see also [23,24]). It was only with the introduction of Multhopp's numerical method [96] that this theory became useful for practical applications. The Multhopp method can be easily implemented in a computer program (for example, see Redeker [103]) that takes the wing planform, twist distribution, and two-dimensional airfoil characteristics as inputs, and calculates the spanwise distributions of induced angle of attack, global lift and moment, and induced drag (the latter is discussed in a following section). The method is readily extended to allow analysis of wings with various flap and aileron deflections (see also Feifel [78]).

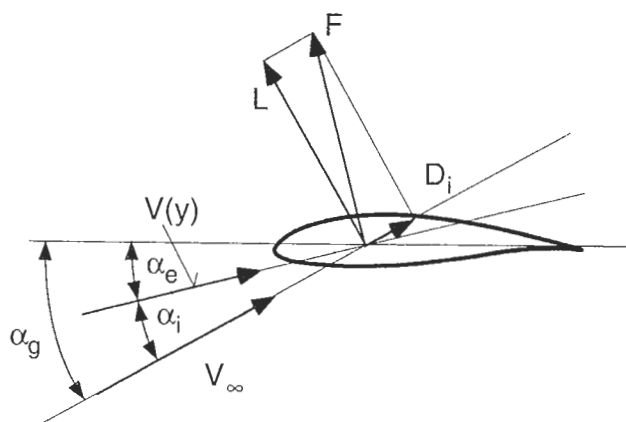


Fig. 20: Local velocity vector $V(y)$ and resulting force vector F at cross section y of a three-dimensional wing (see also Fig. 19).

- α_g geometric angle of attack
- α_e effective angle of attack
- α_i induced angle of attack
- D_i induced drag
- L lift

Induced Drag

According to the Kutta-Joukowski theorem, a vortex placed in a free stream is associated with a force perpendicular to both the local velocity and the vortex line. In the case of a finite-span wing, the direction of the freestream velocity V_∞ is modified by the induced angle of attack α_i . The lift is generated perpendicular to the *local* effective velocity, not the velocity far upstream of the wing. Since the lift and drag of the complete sailplane are defined as forces perpendicular and parallel to the direction of flight (*i.e.* velocity far upstream), the local sectional lift contributes to the drag as well as the lift (Fig. 20). This *induced drag* is an inevitable consequence of the production of lift on a finite-span wing and is present even in an inviscid fluid. According to Prandtl's lifting line theory, the coefficient of induced drag C_{Di} is proportional to the square of the lift coefficient and inversely proportional to the aspect ratio.

The energy lost by the aircraft due to induced drag appears as kinetic energy in the trailing vortex system, particularly in the tip vortices. The tip vortices trail relatively far downstream, gradually dissipating due to viscous effects. All pilots are familiar with the dangers associated with these tip vortices and are trained to follow wake avoidance procedures when operating in the vicinity of large aircraft. An

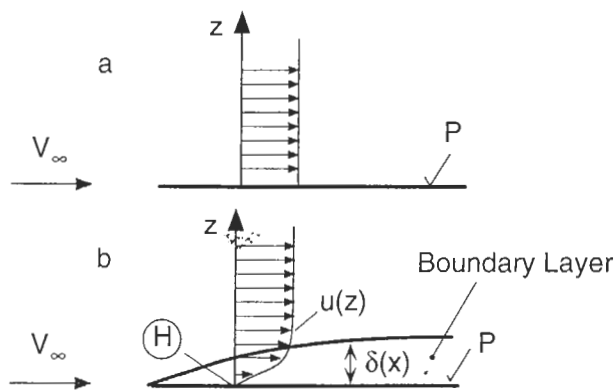


Fig. 21: Flow along a flat plate.

- (a) inviscid flow
- (b) viscous flow
- (H) no slip condition
- $\delta(x)$ boundary-layer thickness
- $u(z)$ velocity profile within boundary layer

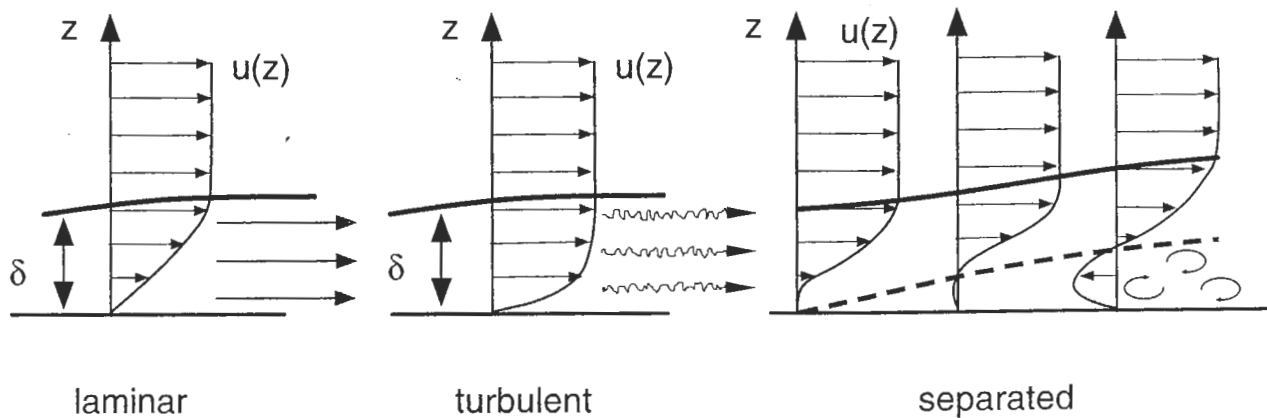


Fig. 22: Velocity profiles $u(z)$ and particle motions for laminar, turbulent, and separated boundary layers.

encounter with the wake turbulence generated by a large transport aircraft can cause loss of control or structural failure [8].

Viscous Effects and Boundary Layers

Laminar and turbulent boundary layers

Although the boundary layer is very thin, extending over only a small portion of the flow field around the aircraft, it plays an important roll in determining a number of aerodynamic characteristics. Drag and separation-related phenomena such as maximum lift coefficient and pitching moment variation can be explained only with reference to boundary-layer theory.

Inviscid flow assumes that the flow field extends to the surface of the body, with no decrease in velocity as the surface is approached. In reality, a boundary layer exists adjacent to the body in which the velocity diminishes from the local potential flow velocity down to zero at the surface (Fig. 21). This so-called *no-slip condition* results from the fact that the air can interact with the surface at a molecular level, even when the surface is highly polished. Starting at zero velocity at the surface, within the boundary layer, the velocity gradually increases from zero at the surface to the velocity predicted by inviscid potential flow. The velocity distribution within the boundary layer is its *velocity profile*. The *boundary-layer thickness* is defined as the dis-

tance from the surface to the location at which the velocity reaches 99% of its local potential-flow value.

Boundary layers are classified as *laminar*, *turbulent*, and *separated*. In a laminar boundary layer, the air particles travel along smooth streamlines parallel to the surface. The velocity varies within the boundary layer, giving rise to shear stresses and loss of kinetic energy in the flow (Fig. 22).

In a turbulent boundary layer, the air particles undergo additional high-frequency velocity variations of a random nature. Although these variations are small compared to the average velocity, they contribute to the energy exchange between the boundary layer and the external flow, as well as within the boundary layer itself. The velocity profile in a turbulent boundary layer is thus "fuller" than that of a laminar boundary layer, exhibiting higher velocities near the surface and a steeper velocity gradient at the surface itself. With increased velocity gradients come increased shear stresses, so that in general, turbulent boundary layers produce higher skin friction than laminar boundary layers.

Separated flow

In the presence of an *adverse pressure gradient* (increasing static pressure), the boundary layer may separate from the surface of the body. The flow travels away from the surface at a *separation point* in a chaotic fashion. Separated flow is often characterized by large-scale unsteady turbulence

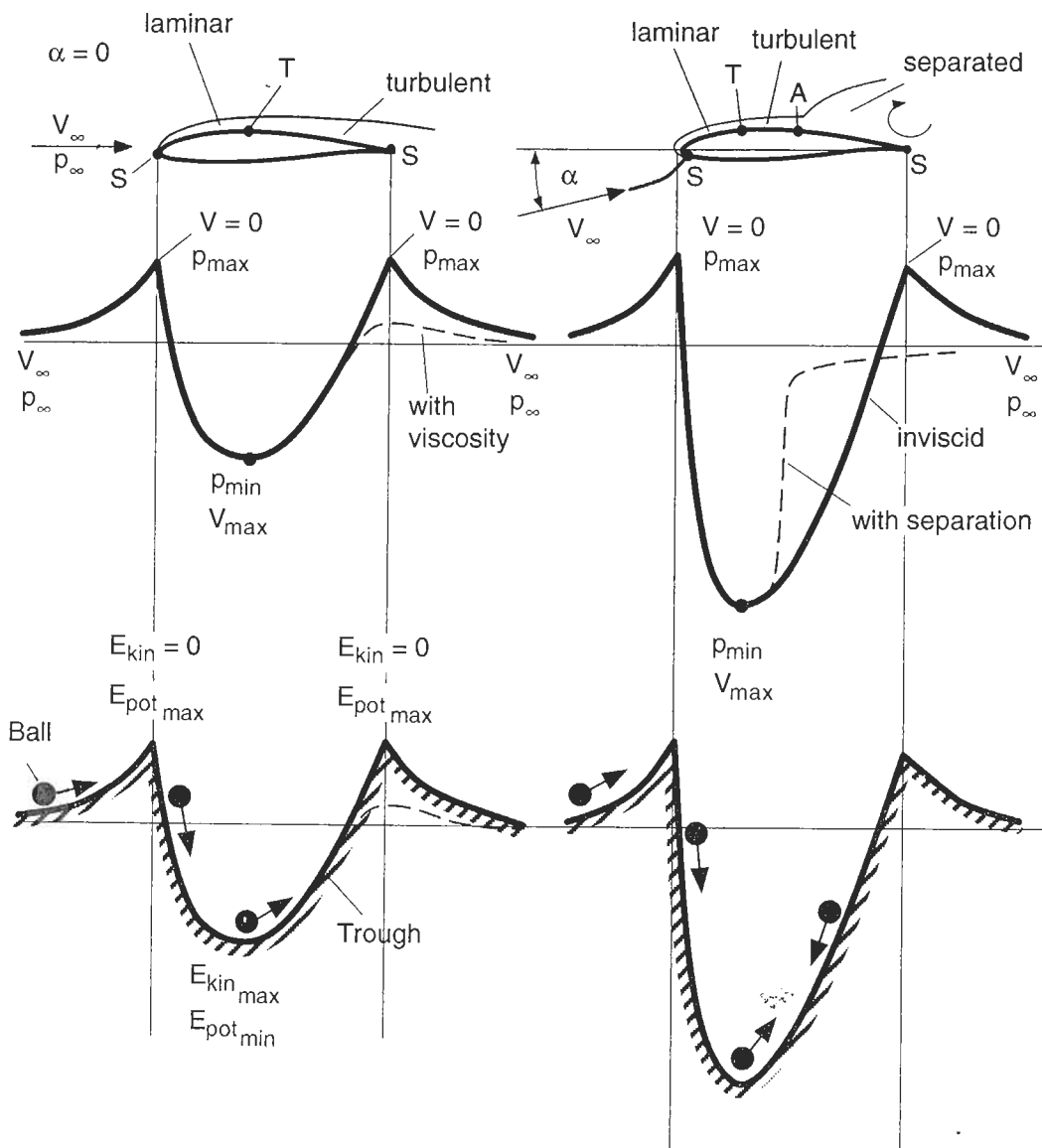


Fig. 23: Pressure distribution on an airfoil with boundary-layer transition and separation:

- S Stagnation point
- T Boundary-layer transition point
- A Point of boundary-layer separation

and mechanical analogy:

- E_{kin} kinetic energy
- E_{pot} potential energy

with no clearly defined streamlines. The velocities near the surface may actually become negative. On the other hand, a laminar boundary layer may separate smoothly, often reattaching shortly downstream of the separation point.

In order to understand the process of separation, consider the path of an air particle near the upper surface of an airfoil (Fig. 23). The particle travels along a streamline that defines the airfoil surface. This streamline originates far upstream of the airfoil and leads to the stagnation point at the leading edge of the airfoil, at which point it splits and extends over the upper and lower surfaces of the airfoil. The streamlines join again at the trailing edge and from there extend downstream of the airfoil.

The pressure distribution along this streamline is a function of the airfoil geometry and angle of attack. Let us consider a typical airfoil (1) at zero angle of attack and (2) at a relatively high angle of attack. In the first case, a flat pressure distribution develops with little variation in pressure. In the second case, however, one observes a very strong pressure gradient and flow separation.

In both cases the flow decelerates from the freestream velocity V_∞ to zero velocity at the forward stagnation point. Subsequently, the flow accelerates and the static pressure decreases to a certain minimum value. In inviscid flow, aft of the point of minimum static pressure, the static pressure increases and the velocity decreases until the trailing edge, where the velocity is theoretically zero. The flow accelerates downstream of the airfoil until it reaches its original (freestream) velocity and static pressure. Thus, a continual exchange between kinetic energy (velocity) and potential energy (pressure) takes place along the streamline.

In viscous flow, however, there are energy losses in the boundary layer. Even when the pressure gradients are weak, the total pressure at the trailing edge will be considerably lower than the freestream total pressure; however, the effect on the overall flow field is minimal. On the other hand, if the adverse pressure gradients aft of the pressure minimum are sufficiently strong, the flow in the boundary layer may decelerate to a full stop and even begin to travel in the reverse direction. That is, the flow separates.

Separation may be visualized with the help of a simple physical analogy. A ball rolled with initial velocity V along a curved track with the same shape as the airfoil's pressure distribution will experience an exchange between kinetic and potential energy analogous to that experienced by the air particles. If the ball loses energy through friction, it may come to a halt before the second peak, failing to reach the

top and rolling back towards the low point in the path. In the analogy, this corresponds to flow separation.

Separation occurs in sailplanes wherever sufficiently strong adverse pressure gradients are encountered. These are always present on wings at high angles of attack and limit the maximum attainable lift. At the same time, the airfoil drag increases due to changes in the static pressure distribution. Strong adverse pressure gradients are also found on the aft faces of blunt bodies such as landing gear and dive brakes, leading to local flow separation and substantial increases in drag.

Boundary-layer transition

The boundary layer over a sailplane wing begins as laminar and attached, and may progress in sequence to lam-

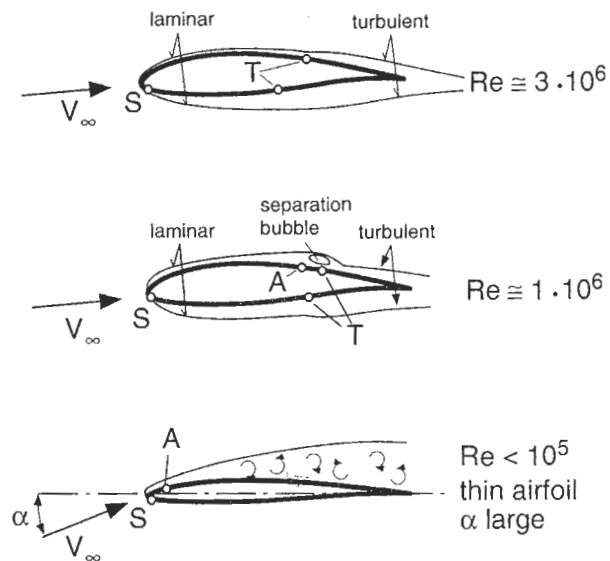


Fig. 24: Behavior of laminar boundary layer under various pressure distributions and Reynolds numbers:

- Transition
- Separation bubble
- Laminar separation
- S Stagnation point
- A Separation point
- T Boundary-layer transition

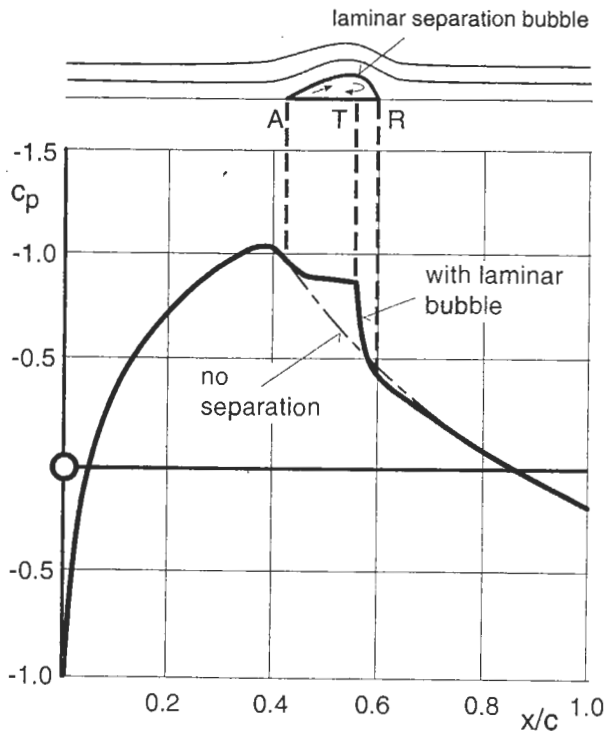


Fig. 25: Pressure distribution in the vicinity of a laminar separation bubble measured on an FX 66-S-196 V1 airfoil by J. H. M. Gooden [181]. Upper surface pressure distribution corresponding to $\alpha = -1.0^\circ$ and $Re = 0.49 \cdot 10^6$.

A separation point
 T transition point
 R reattachment point

laminar/separated, turbulent, and turbulent/separated. At the forward stagnation point, where the boundary layer forms, the flow is normally laminar. However, the laminar flow is only stable under certain conditions, so that in general the boundary layer will transition to a turbulent state after a certain distance. Both laminar and turbulent boundary layers may separate in the presence of an adverse pressure gradient along the direction of flow. However, since turbulent boundary layers are characterized by increased energy transfer with the flow outside the boundary layer, they are better able to overcome adverse pressure gradients without separation. Laminar boundary layers, on the other hand, may separate in the presence of relatively small

adverse pressure gradients. Depending on the local flow conditions, a laminar boundary layer may separate permanently or become turbulent while separated and reattach. The latter case is accompanied by the formation of a so-called *laminar separation bubble* (Figs. 24,25).

Whether and where these phenomena occur depends on the following parameters:

- Pressure distribution (Airfoil geometry and angle of attack)
- Reynolds number
- Surface quality (smoothness, waviness, contamination by rain, snow, ice or insects)
- Level of turbulence in the oncoming flow

The following factors help maintain laminar flow:

- Favorable pressure gradients, for example in the area of the leading edge
- Low Reynolds numbers, for example as observed on model airplanes and birds
- High surface quality with no roughness, waviness, or contamination (as typical of modern fiberglass sailplanes)
- Low turbulence in the oncoming flow, for example in flight or in laminar wind tunnels.

While low frequency atmospheric turbulence presents no problem in this respect, the high frequency turbulence typical of many wind tunnels can have a significant effect on boundary-layer development.

A sound physical understanding of boundary-layer transition phenomena is a prerequisite to the design of high performance sailplane airfoils. Since skin-friction coefficients are so much lower when the boundary layer remains laminar, it is important to ensure that boundary-layer transition occurs as far back on the airfoil as possible. Separation, on the other hand, incurs large drag penalties, and for this reason care must be taken to ensure that the transition occurs before the boundary layer can separate. This is accomplished by tailoring the airfoil geometry, and, where required, by means of special devices such as "zig-zag tape" or pneumatic turbulators (Fig. 26; see also [72, 166, 168, 183-185, 192]). It is especially difficult to develop airfoil shapes with extensive laminar flow

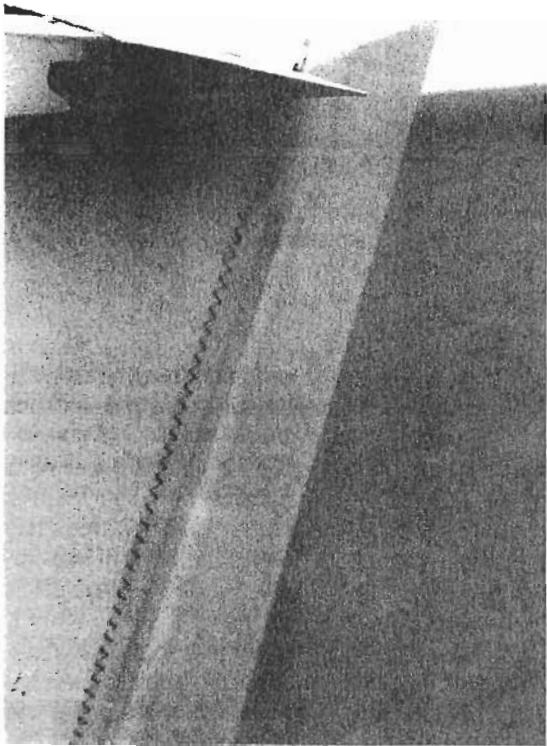
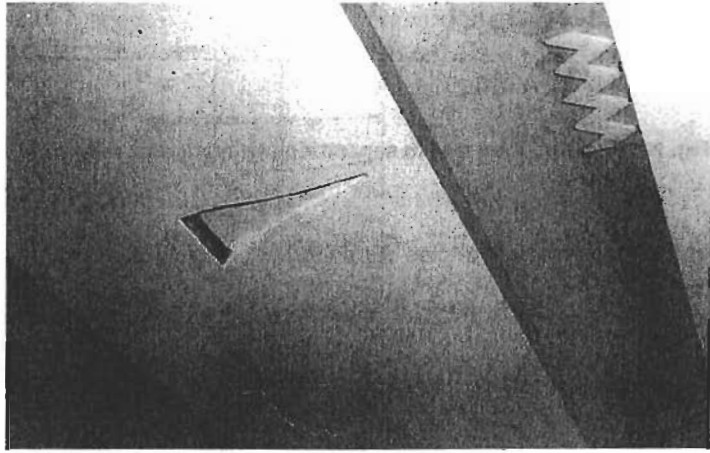
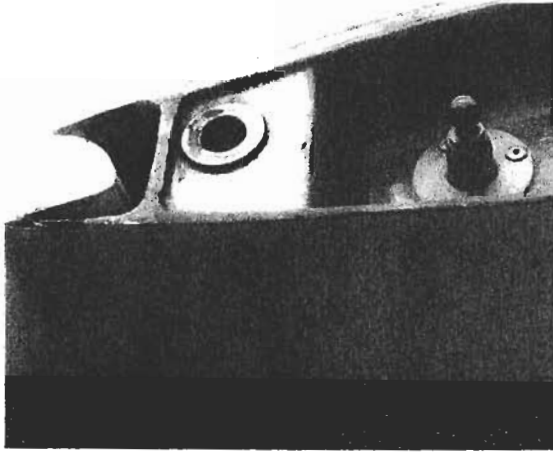


Fig. 26: Boundary-layer tripping devices (turbulators) have become a common sight on modern sailplanes. Above left, "zig-zag" tape bonded to the airfoil underside just ahead of the aileron (Nimbus 4 inner wing panel). The tape terminates just before the end of the wing panel to allow the gap to be properly taped during assembly. Left, zig-zag tape on vertical stabilizer, in this case integrated with the rudder hinge gap seal. Above right, ASW-27 outer wing section lower surface. Here, laminar flow extends onto the aileron itself. The boundary layer is tripped by means of a series of blow-holes arranged spanwise along the aileron lower surface. The holes communicate with a plenum that receives air either from a small Pitot tube or (in this case) a NACA-inlet. The short length of zig-zag tape upstream of the inlet improves inlet efficiency by energizing the boundary layer.



Fig. 27: Pressure drag due to separation (cylinder) and skin-friction drag due to boundary layer (flat plate)

at both low and high angles of attack (that is, both in high speed and thermaling flight). See also R. Eppler [176] for an empirical approach to the prediction of boundary layer transition.

Friction drag and pressure drag

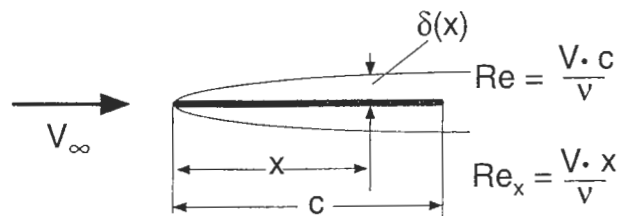
The shear stresses associated with the boundary layer act in a direction parallel to the local surface; when integrated over the entire surface of an aircraft or an airfoil, they yield the *friction drag*. Similarly, the local static pressure also acts on the aircraft surface, albeit *perpendicular* to the local surface. The integrated effect of the static pressure includes a drag component termed the *pressure drag* (Fig. 27).

Separated flow, whether over a stalled airfoil or an unfaired strut, can be a significant source of pressure drag. Even if there is no flow separation, the shear forces within the boundary layer can have an adverse effect on the static pressure distribution, providing a further source of pressure drag. The induced drag of a finite-span wing may also be categorized as a form of pressure drag. Other significant sources of pressure drag include unfaired landing gear, antennas, exposed control linkage, extended dive brakes, localized areas of separation about the wing-fuselage junction, the empennage, and unsealed control surface hinge gaps.

Friction drag is present with both laminar and turbulent boundary layers. Consider a flat plate oriented parallel to the freestream. In the inviscid potential flow solution, the static pressure along the plate is constant, allowing the boundary layer to be examined free of influence from pressure gradients or flow separation. For this reason the flat plate is a popular model for both theoretical and experimental boundary-layer research. Of particular interest are the results relating the boundary layer thickness and

Table 3: Theoretical drag coefficients and boundary-layer thicknesses for flat plates. See also Schlichting [22], Chapters 7 and 21.

	laminar	turbulent
drag coefficient, c_d (both sides)	$2 \frac{1.328}{\sqrt{Re}}$	$2 \frac{0.074}{\sqrt[5]{Re}}$
boundary-layer thickness $\delta(x)$	$\frac{5x}{\sqrt{Re_x}}$	$\frac{0.37x}{\sqrt[5]{Re_x}}$



friction drag, both of which are functions of Reynolds number. Analytic results for these quantities are presented in Table 3.

For example, for a flat plate 1m long subject to a freestream velocity of 30m/s, these formulas yield a boundary-layer thickness of 3.5mm (laminar boundary layer) or 20mm (turbulent) at the trailing edge. The corresponding Reynolds number ($Re = 2 \cdot 10^6$) is typical of sailplane airfoils.

The friction drag as calculated by these formulas is presented graphically in Fig. 28. In order to facilitate comparison with data from actual airfoils, the results are presented for a two-sided flat plate. At low Reynolds numbers, the boundary layer remains laminar over the entire plate. Conversely, at very high Reynolds numbers the drag contribu-

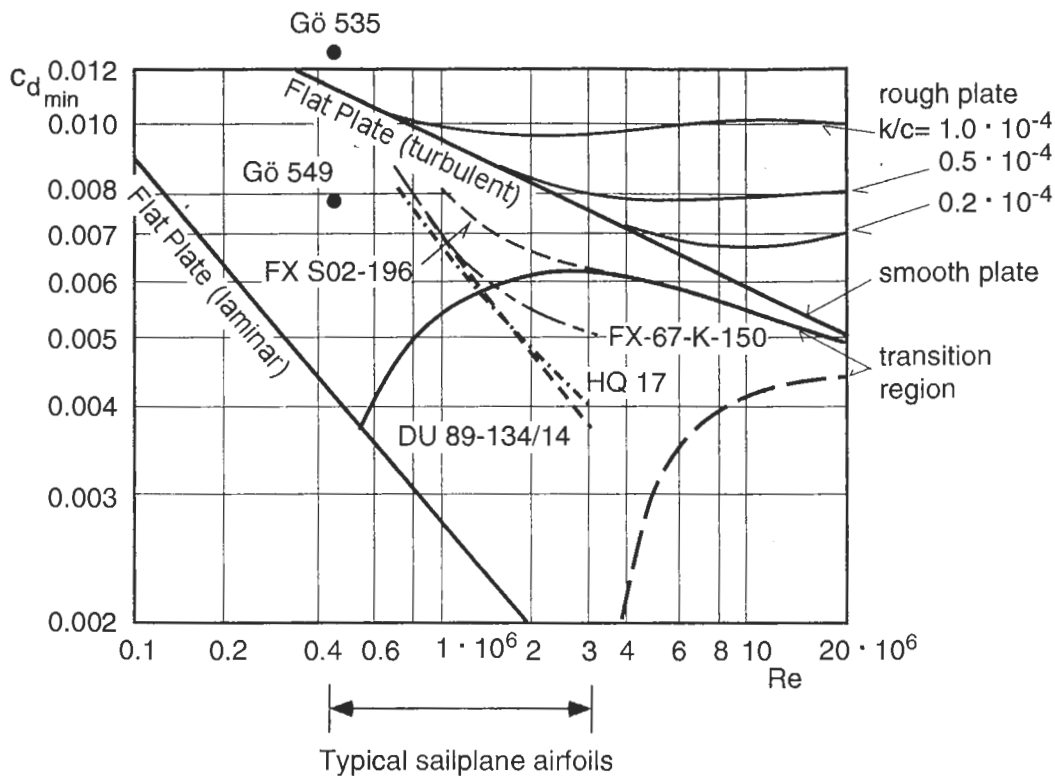


Fig. 28: Skin friction drag of two-sided flat plate as a function of Reynolds number, compared with minimum drag coefficients of some typical airfoils.

- Transition region, high turbulence environment (typical wind tunnel)
- - - Transition region, low turbulence wind tunnel or free atmosphere

tion from the initial laminar portion of the boundary layer is negligible, and the drag approaches the value obtained by assuming a completely turbulent boundary layer. Sailplane airfoils typically operate in a transition region where both the laminar and turbulent portions of the boundary layer contribute significantly to the total drag. It is apparent that where the boundary layer is primarily turbulent, the drag is much higher than would be observed with a primarily laminar boundary layer. Low drag requires the boundary layer to remain laminar to the greatest extent possible.

Figure 28 includes data for a few sailplane airfoils for reference. The airfoil data differ considerably from the simple flat plate results because of the static pressure variations present along the airfoil surfaces. More detailed airfoil analysis may be performed using one of several modern soft-

ware tools for the detailed design and analysis of airfoils. One well-known program by Eppler [177,180] is specifically intended for use in the design of airfoils for special applications ("airfoil tailoring"). This program computes the lift, drag, and pitching moment coefficients of prescribed airfoils as a function of Reynolds number and angle of attack. Boundary-layer effects are included. The program also solves the inverse problem (determining the airfoil shape required to achieve a prescribed velocity distribution). Another well-known program is XFOIL by M. Drela [173], an interactive, graphical design and analysis tool with similar capabilities, including viscous analysis of existing airfoils, prediction of boundary-layer transition, laminar separation bubbles, turbulent separation, solution of inverse problem, and rapid evaluation of airfoil modifications.

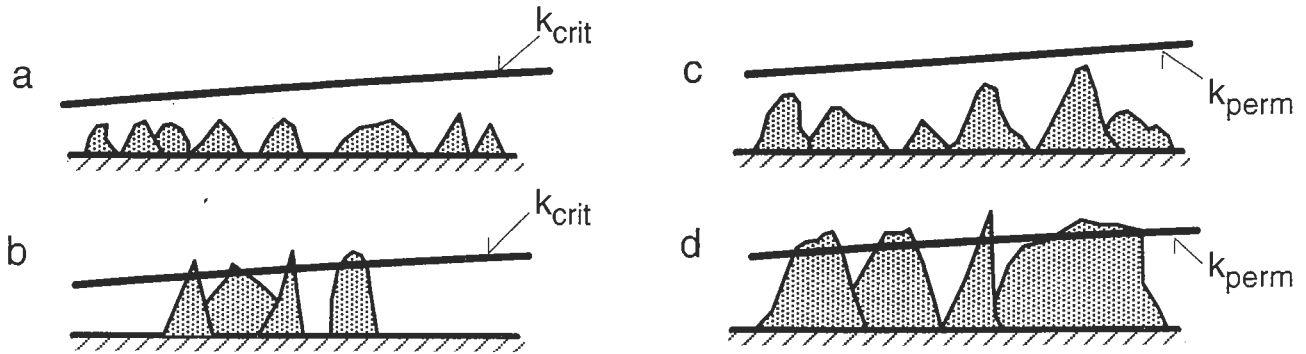


Fig. 29: Effect of surface roughness on laminar (a,b) and turbulent (c,d) boundary layer.

- | | |
|--------------------------------|------------------------------------|
| a) no effect | c) hydraulically smooth |
| b) transition due to roughness | d) increased drag due to roughness |

Importance of surface quality

Irregularities on the surface of a flat plate or airfoil affect laminar and turbulent boundary layers in different ways.

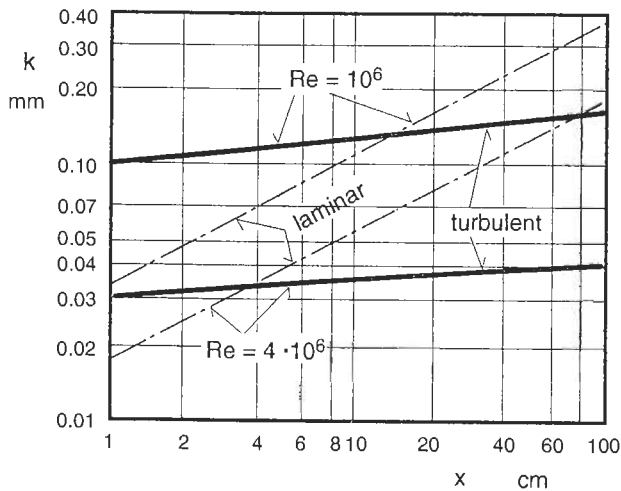


Fig. 30: Critical and permissible surface roughness as a function of boundary-layer length per F. X. Wortmann [115]. Reference length for Reynolds number is $c = 1\text{m}$.

Surface roughness is essentially a field of small amplitude irregularities. In a laminar boundary layer, if the irregularities exceed a certain maximum height, the flow may become turbulent. This maximum tolerable roughness is termed the *critical roughness* and is a function of the Reynolds number and pressure distribution. For a flat plate, the critical roughness k is given by the following formula:

$$\frac{k_{\text{crit}}}{\delta} = \frac{2.4}{\sqrt[4]{Re_x}} \quad \text{Critical Roughness} \quad (21)$$

This means that the roughness must not exceed a value of 1/10 to 1/15 the local boundary-layer thickness. If the roughness remains below this value, it has no influence on the laminar boundary layer or the drag (Fig. 29).

For turbulent boundary layers, the drag begins to increase as soon as the roughness exceeds a minimum significant value, known as the *permissible roughness*. The permissible surface roughness is also a function of Reynolds number:

$$\frac{k_{\text{perm}}}{x} = \frac{100}{Re_x} \quad \text{Permissible Roughness} \quad (22)$$

If the roughness is less than the permissible roughness, the surface is considered *hydraulically smooth*. If

the roughness is greater than k_{perm} , the drag varies directly with the degree of roughness, as shown in Fig. 28. In the presence of pressure gradients, however, the surface friction coefficients may vary considerably from their flat plate values.

Figure 30 presents a simple surface roughness diagram developed by F. X. Wortmann [115] for use with sailplanes. The figure presents the critical surface roughness (laminar boundary layers) and permissible surface roughness (turbulent boundary layers) as a function of boundary-layer length and Reynolds number. It is evident that surface roughness as small as 1/100 to 1/10 mm may be detrimental. Surface waviness has a similar effect. Sailplane manufacturers and pilots therefore devote considerable effort to achieving and maintaining a high surface quality. Even raindrops or insects can lead to premature transition. Airfoils vary considerably, however, in their sensitivity to such surface contamination.

Concluding Remarks

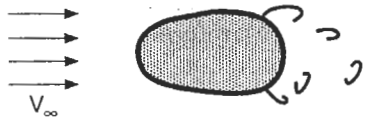

The preceding sections reviewed the basics of fluid mechanics relevant to sailplane design. A mathematical presentation has been deliberately avoided; rather, emphasis has been placed developing a physical understanding of the most important phenomena such as the production of lift and drag. A sound understanding of the physics of the problem is essential, for only then can one take advantage of the full range of design possibilities.

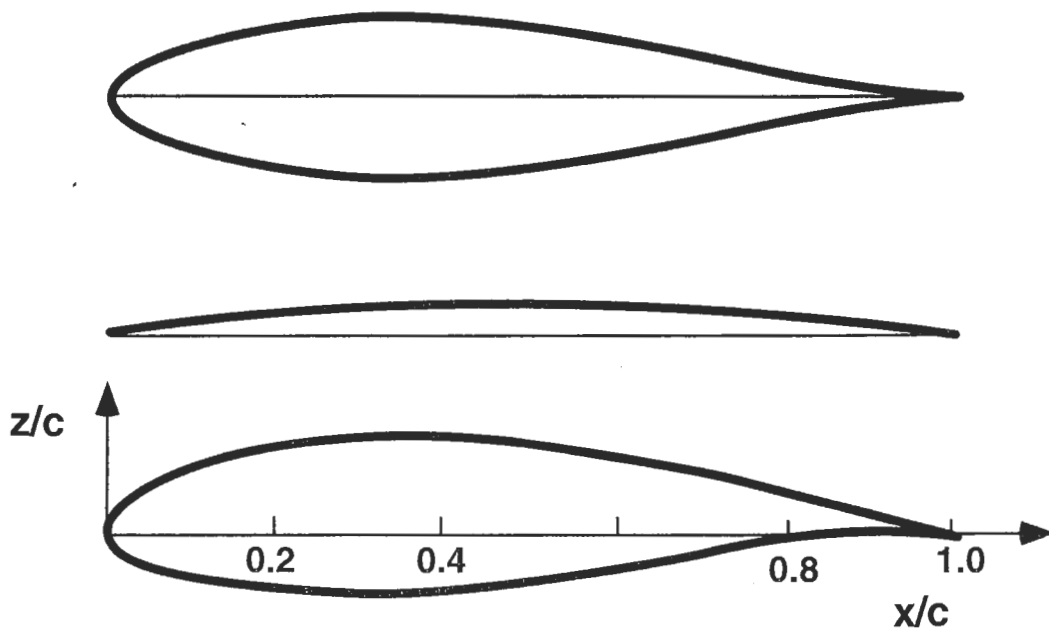
This level of understanding is also valuable when interpreting wind-tunnel and flight-test data. These experimental results often reveal surprising and unexpected phenomena, and a good understanding of the basics helps in developing solutions to unforeseen aerodynamic problems.

The "big picture" is especially important when surveying the extensive technical literature in aerodynamics, as it allows ready identification of material having relevance to sailplane design. Table 4 presents a summary overview of the main topics in fluid mechanics, outlining the manner in which the complex fundamental equations are reduced to the simpler relationships used in sailplane design.

For more detailed presentations of aerodynamic theory, the reader is referred to texts such as H. Schlichting and E. Truckenbrodt [24], J. D. Anderson [3, 4], and M. Kueth and C. Chow [15]. See also R. T. Jones [14] for a concise overview of wing theory.

Table 4: Overview of topics in fluid mechanics.

Fluid Mechanics, general case:	
	
Compressible, viscous flow: Navier-Stokes Equations Gas laws Continuity Equation	
Flow at high Reynolds numbers ($Re > 10^5$):	
	
Inviscid compressible flow: Nonlinear potential equation	Viscous compressible boundary layer: Compressible boundary-layer theory
Low Mach numbers and High Reynolds numbers ($M < 0.3$, $Re > 10^5$):	
Inviscid incompressible flow:	Viscous incompressible boundary layer:
Linear potential equation: Elementary solutions: Potential vortices and sources, Superposition principle	Boundary-layer theory: Laminar, turbulent, and separated boundary layers
Airfoil theory: Pressure distribution, lift, moment	Transition, separation, influence of Reynolds number and surface quality
Wing theory: unswept wing with large aspect ratio, Prandtl lifting-line theory	Friction drag, pressure drag, maximum lift
Lift distribution Induced drag	



x/c	0.01	0.05	0.10	0.15	0.20	0.30	0.40	0.50	0.60	0.70	0.80	0.90	0.95	1.0
$100 \cdot z_u/c$	2.6	5.6	7.9	9.3	10.4	11.8	12.1	11.3	9.7	7.5	5.1	2.5	1.3	0
$100 \cdot z_l/c$	-1.3	-3.2	-4.3	-5.1	-5.6	-6.0	-5.6	-4.6	-3.2	-1.7	-0.3	0.6	0.6	0

Fig. 31: Form, camber line, and geometry for NACA 63₃ - 618

Airfoil and Wing Theory

Wing/Airfoil Geometry and Aerodynamic Coefficients

Airfoil geometry

Since an airfoil is a cross section of a wing in the plane defined by $y = \text{constant}$, the airfoil geometry is defined only in terms of the coordinates x and z . The airfoil geometry is typically presented as a table of chordwise locations x and corresponding upper and lower coordinates z_u and z_l . In order to make this information independent of the size of the airfoil and the choice of dimensional units, the coordinates are normalized to the airfoil chord, c (Fig. 31). The coordinates are presented as x/c and z/c , the values

of which range from zero to unity.

Every airfoil can be defined as a combination of a thickness distribution and a camber line (mean line). The chord is the distance between the endpoints of the camber line. The 1/4-chord point, the point on the chord line lying one quarter of the chord length aft of the leading edge, plays an important role as a reference point for the aerodynamic pitching moment. The angle of attack is the angle between the chord line and the direction of freestream flow.

Although a fairly large set of coordinates is required to specify the airfoil geometry to a sufficient degree of precision, to a certain extent airfoils can be characterized using just a few parameters. These are the maximum thickness, the location of the point of maximum thickness, the maximum camber, location of maximum camber, the leading-edge radius, and the trailing-edge angle (included angle at the trailing edge). These parameters are illustrated in

Fig. 32. Usually these are normalized to the airfoil chord in the same manner as the coordinates.

Wing geometry

A complete description of the wing includes not only the airfoil geometry, but the wing planform and the spanwise airfoil variation as well.

In most cases, the leading and trailing edges of sailplane wings consist of straight line segments. Thus, the basic sailplane wing planforms are rectangular, tapered, rectangular/tapered, and double or triple tapered (Fig. 33). Mention may also be made of the elliptical wing, which, although seldom used in modern sailplanes, is of great theoretical importance in wing theory. Most of the effects of wing planform can be expressed as a function of two geometric parameters: the *aspect ratio* and the *taper ratio*, defined as follows (Fig. 34):

$$AR = b^2/S \quad \text{Aspect Ratio} \quad (23)$$

$$\lambda = c_t/c_r \quad \text{Taper Ratio} \quad (24)$$

For a rectangular wing, the aspect ratio is simply the ratio of the span to the chord ($AR = b/c$). In the case of the rectangular-tapered and double-tapered wing, the location of the taper break and the taper ratios of the inner and outer portion of the wing are required to complete the definition of the wing geometry.

Most sailplane wings are unswept or only slightly swept. It should be kept in mind that if the wing is both swept and

tapered, the sweep angles of the leading edge and the 1/4-chord line (the locus of points located at $x/c = 1/4$) are different. The angle between the wing and the y axis is the *dihedral*.

Another important geometric parameter is the *twist*, the spanwise variation of the geometric angle of attack (Fig. 34). The angle about the y axis between a reference line in the wing (for example, the wing chord line on its plane of symmetry) and the reference axis of the fuselage is the *wing angle of incidence*.

The geometry of the tail surfaces is defined using similar parameters.

Pressure coefficient

The pressure distribution over an airfoil and its importance to the development of the boundary layer has already been discussed. When considering the pressure distribution, it is useful to present the pressure as a nondimensional *pressure coefficient*. This is the differential pressure between the static pressure p at a particular location in the flow field and the static pressure p_∞ far upstream of the aircraft, normalized to the dynamic pressure q_∞ :

$$c_p = \frac{p - p_\infty}{q_\infty} \quad \text{Pressure coefficient} \quad (25)$$

$$q_\infty = \frac{\rho}{2} V_\infty^2 \quad \text{Dynamic pressure} \quad (26)$$

Upon application of Bernoulli's equation to the local velocity u , the pressure coefficient can be expressed as

$$c_p = \frac{p - p_\infty}{q_\infty} = 1 - \left(\frac{u}{V_\infty} \right)^2 \quad (27)$$

The pressure coefficient c_p is used primarily to present calculated or measured airfoil pressure distributions (Fig. 35). Conventionally, in figures such as Fig. 35, negative pressures are plotted in the positive direction of the vertical axis. In nondimensional terms, the pressure coefficient at the stagnation point in incompressible flow is exactly 1. The differential pressure Δc_p between the upper and lower sides of the airfoil is a function of the chordwise coordinate x .

Aerodynamic coefficients

The total aerodynamic force acting on a wing or airfoil may be resolved into components perpendicular and parallel to

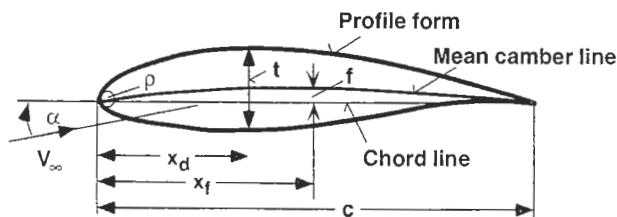


Fig. 32: Airfoil geometric parameters.

- t thickness
- x_d location of maximum thickness
- f camber
- x_f location of maximum camber
- ρ leading-edge radius
- c chord

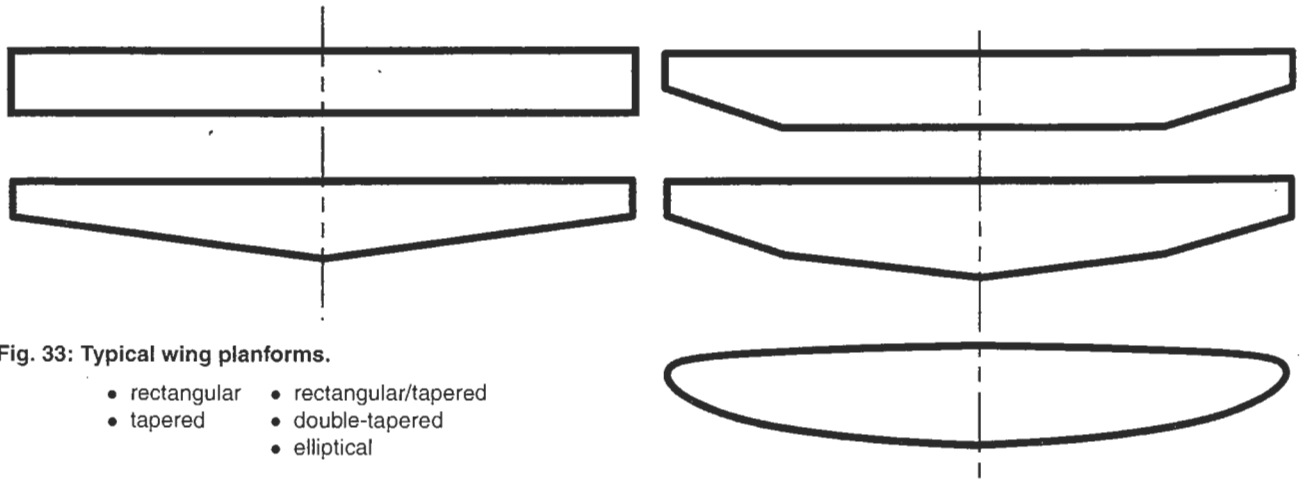
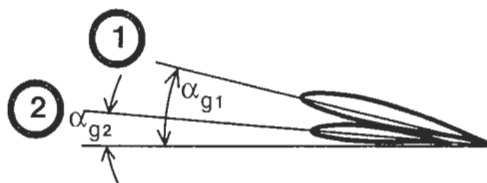
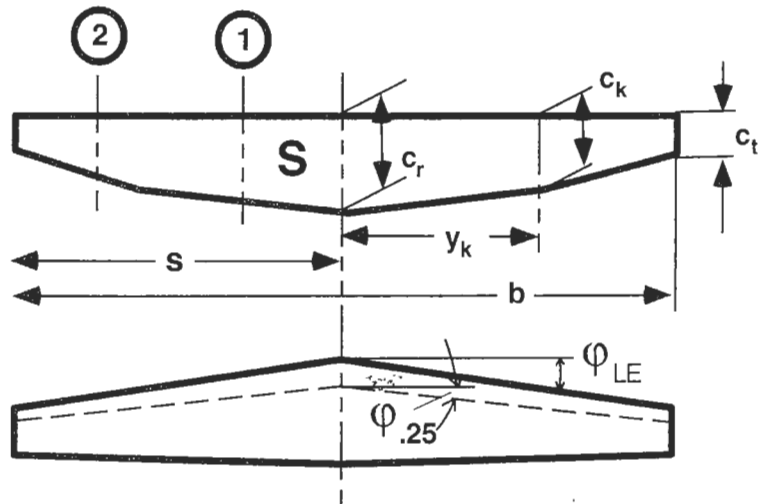


Fig. 33: Typical wing planforms.

- rectangular
- tapered
- rectangular/tapered
- double-tapered
- elliptical

Fig. 34: Wing geometric parameters.

- b span
- s semispan
- c_r root chord
- c_t tip chord
- ϕ_{LE} leading-edge sweep angle
- $\phi_{.25}$ sweep angle of 1/4-chord line
- S wing area
- y_k spanwise location of taper change point
- c_k chord at taper change point
- $\alpha_g(y)$ wing twist



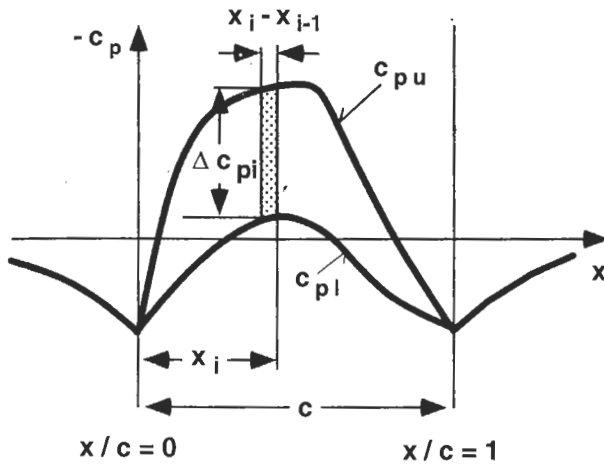


Fig. 35: Nondimensional pressure distribution over airfoil.

Δc_{pi} pressure difference between upper and lower surface at x_i

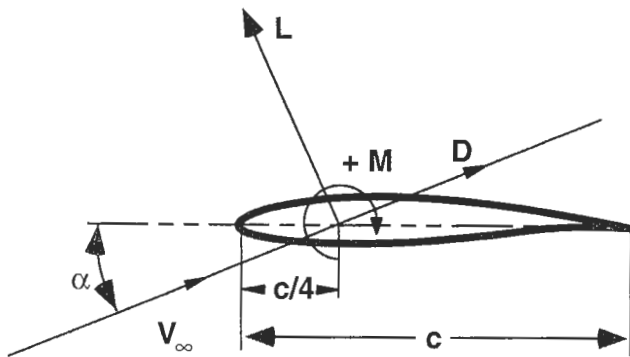


Fig. 36: Aerodynamic forces and moment on an airfoil.

L Lift D Drag M Pitching moment

the flow velocity together with a moment about a prescribed reference point. The three quantities are *lift*, *drag*, and *pitching moment*, respectively. The pitching moment is referenced to a specified point on the airfoil, usually at the 1/4-chord point, and the lift and drag may be thought of as being applied at this location (Fig. 36). If the pitching moment tends to increase the angle of attack of the wing, it is defined as positive, or "nose-up".

As with the pressure coefficients, the lift, drag, and pitch-

ing moment of a two-dimensional airfoil are expressed as nondimensional coefficients. The reference quantities are the free stream dynamic pressure, q_∞ , and the chord c :

$$c_l = l/q_\infty c \quad \text{Sectional Lift Coefficient} \quad (28)$$

$$c_d = d/q_\infty c \quad \text{Sectional Drag Coefficient} \quad (29)$$

$$c_m = m/q_\infty c^2 \quad \text{Sectional Pitching Moment} \quad (30)$$

These coefficients also define the local sectional loads, that is, the lift, drag, and pitching moment per unit span of the wing. For example, $c_l(y)$ denotes the lift distribution along the span of the wing.

Similar definitions apply to the global (total) forces acting on a wing:

$$C_L = L/q_\infty S \quad \text{Lift Coefficient} \quad (31)$$

$$C_D = D/q_\infty S \quad \text{Drag Coefficient} \quad (32)$$

$$C_M = M/q_\infty S c \quad \text{Pitching Moment} \quad (33)$$

As will be discussed, a suitable reference chord c must be chosen for non-rectangular wings.

The sectional lift coefficient c_l is obtained by integrating the pressure difference between the upper and lower airfoil surfaces over the entire chord:

$$c_l = \int_0^1 \Delta c_p(x) d(x/c) \approx \sum_{i=1}^n \Delta c_{pi} (x_i - x_{i-1})/c \quad (34)$$

Experimental and theoretical aerodynamic characteristics are typically presented in a format such as that of Fig. 37 in order to highlight the variation of the aerodynamic coefficients with the angle of attack. Pitching moment data are presented as a function of lift coefficient in order to simplify stability analysis.

The figure shows that at moderate angles of attack, the lift and pitching moment coefficients exhibit a linear relationship with angle of attack. Above a certain value of angle of attack, these coefficients depart from their linear relationships due to flow separation. In the linear region, the lift and pitching moment coefficients are expressed as follows:

$$c_l = \frac{dc_l}{d\alpha} (\alpha - \alpha_0) \quad (35)$$

$$c_m = \frac{dc_m}{dc_l} c_l + c_{m_0} \quad (36)$$

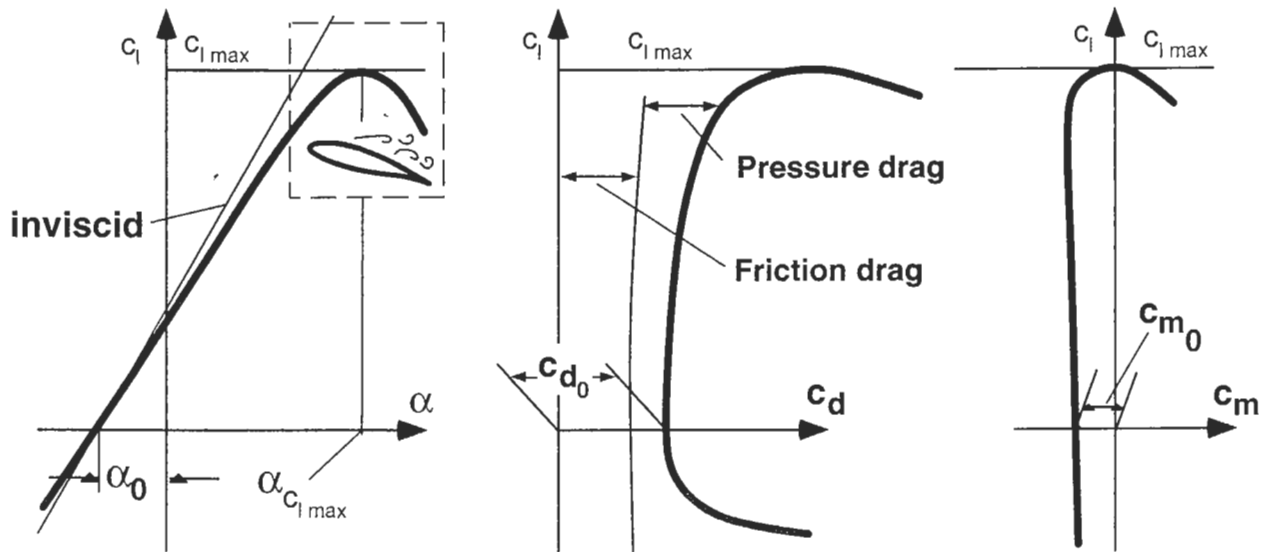


Fig. 37: Aerodynamic forces and moment on an airfoil as a function of angle of attack and lift coefficient

The linear representation of the lift and moment curves therefore depends on following four parameters:

- $\frac{dc_l}{d\alpha}$ Lift-curve slope
- $\frac{dc_m}{dc_l}$ Moment gradient
- α_0 Zero-lift angle of attack
- c_{m_0} Zero-lift moment

The lift-curve slope determines how rapidly the lift coefficient increases with angle of attack. For this purpose the angle of attack is usually expressed in radians.

Zero-lift angle of attack and zero-lift moment are illustrated in Fig. 38. If the airfoil is symmetrical (and, in the case of a three-dimensional wing, if the wing is untwisted), both the zero-lift angle of attack and zero-lift moment are zero. If the airfoil is cambered (or the wing twisted), these parameters are generally non-zero (Fig. 38). An exception here would be a cambered airfoil with a reflexed mean line.

These four parameters in the linear airfoil model lend themselves to theoretical calculation since they are not strongly influenced by viscous effects. While the lift-curve

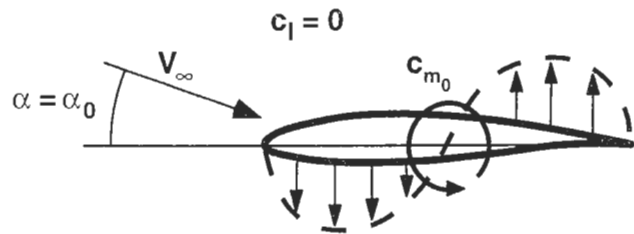


Fig. 38: Zero-lift moment on cambered airfoil.

slope and moment gradient are relatively independent of the actual airfoil shape, the zero-lift angle of attack and pitching moment are strong functions of the airfoil camber. As the camber increases, these quantities become increasingly negative in value.

Thin airfoils in inviscid flow have a theoretical lift-curve slope of 2π (6.28) per radian. In practice, viscous effects tend to reduce the lift-curve slope while thickness tends to increase it. For the relatively thick airfoils commonly used on sailplanes, the actual sectional value of the lift-curve slope is fairly close to this idealized value.

As will be shown, the lift-curve slope of a three-dimensional wing is also a function of its aspect ratio.

Due to the pronounced influence of turbulence, airfoil drag and maximum lift coefficient can only be measured in low-turbulence wind tunnels or in flight test.

Aerodynamic center and center of pressure

The pitching moment gradient dc_m/dc_l is affected by the choice of the moment reference point. This is evident in Fig. 39, which compares moment curves obtained using various reference points. The figure assumes that the lift acts at a fixed location (this is in fact the case for a symmetrical airfoil). If the airfoil leading edge is chosen as the moment reference point, a pitching moment will result, becoming increasingly negative (nose-down) as the lift increases. On the other hand, if the moment is calculated about the trailing edge, the pitching moment will become increasingly positive (nose-up) as the lift increases. Between the leading and trailing edges there exists a particular reference point about which the moment remains constant as the lift varies, that is, the moment gradient is zero. This reference point, the *aerodynamic center*, is of particular interest to the study of aircraft stability and control, and is defined by the following relationship:

$$\frac{dc_{m_{ac}}}{dc_l} = 0 \quad (37)$$

Here the subscript "ac" indicates that the aerodynamic center is used as the reference point for the moments.

Since the pitching moment about the aerodynamic center does not vary with angle of attack, it is identical to the zero-lift moment. The aerodynamic forces on an airfoil may therefore be broken down into a constant pitching moment c_{m_0} about the aerodynamic center, and a lift applied at the aerodynamic center, varying with the angle of attack α (Fig. 40). This result applies only to the linear region of the lift and moment curves, that is, no flow separation. Slight variations may arise even in the linear operating range due to viscous effects.

Thin airfoil theory predicts that the aerodynamic center is located precisely at the airfoil 1/4-chord, that is,

$$\frac{x_{ac}}{c} = 0.25 \quad (38)$$

$$c_{m_{ac}} = c_{m_{1/4}} \quad (39)$$

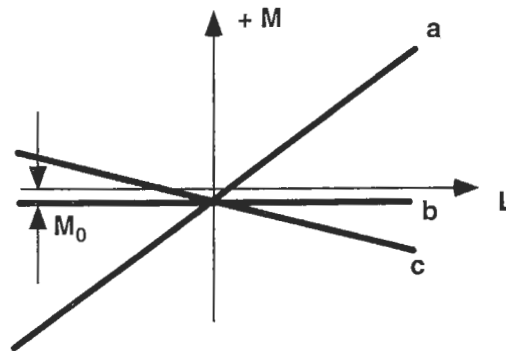
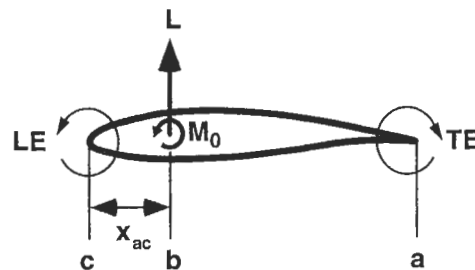


Fig. 39: Effect of moment reference point on pitching moment gradient.

Reference point at: a) trailing edge (TE)
b) aerodynamic center
c) leading edge (LE)

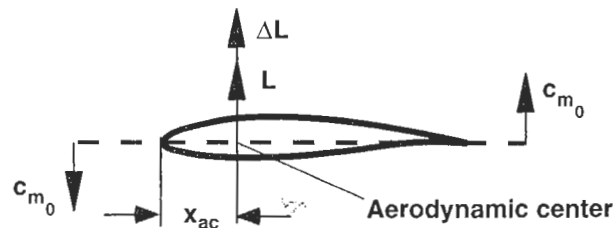


Fig. 40: Aerodynamic center and zero-lift moment.

Here the "1/4" subscript indicates that moments are measured about the airfoil 1/4-chord. In practice, the aerodynamic center may vary slightly from the 1/4-chord location, in which case the relationship becomes:

$$c_{m_{1/4}} = c_{m_0} + \left(\frac{1}{4} - \frac{x_{ac}}{c} \right) c_l \quad (40)$$

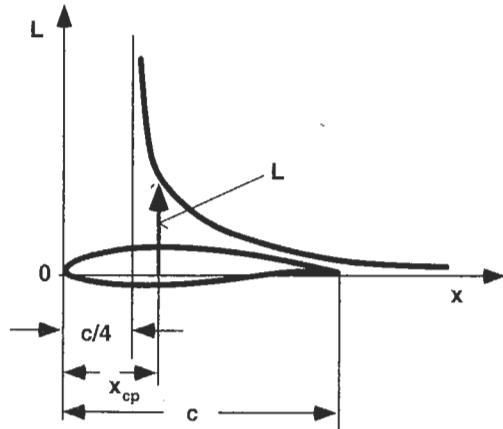


Fig. 41: Variation of center of pressure

Not to be confused with aerodynamic center is the *center of pressure*. This is the point on the airfoil at which the lift acts; that is, the reference point about which the pitching moment is zero. For symmetrical airfoils ($c_{m_0} = 0$), the center of pressure coincides with the aerodynamic center at the 1/4-chord. In the case of cambered airfoils ($c_{m_0} \neq 0$), the center of pressure varies with lift coefficient, migrating forward from infinity towards the 1/4-chord point as the lift coefficient is increased (Fig. 41). The center of pressure is rarely used in stability analyses; modern practice favors the aerodynamic center as a reference point for describing airfoil properties.

Geometric aerodynamic center and mean aerodynamic chord

Since the aerodynamic center is of great significance in stability analysis, it is useful to define an aerodynamic center for a three dimensional wing as well. In practice, viscous effects cause the aerodynamic center to vary from its theoretically determined position, and a distinction must be made between the geometric aerodynamic center and the experimentally measured aerodynamic center. The geometric aerodynamic center of a wing is analogous to the 1/4-chord point of an airfoil, and, accordingly, the geometric aerodynamic center of a rectangular wing lies along its 1/4-chord line.

If the wing is tapered or swept, an equivalent rectangular

wing may be defined, having the same forces and moments of the original wing. The 1/4-chord line of the rectangular wing corresponds then to the aerodynamic center of the actual wing. The geometry of the equivalent wing is determined by imagining the 1/4-chord line of the original wing as a beam loaded with weights proportional to the local chord (Fig. 42). The geometric aerodynamic center is then the center of gravity of this structure. The chord of the equivalent rectangular wing, the *mean aerodynamic chord*, is based on the chord of the original wing:

$$m.a.c. = c_{\mu} = \frac{1}{S} \int_{-s}^{+s} c^2(y) dy \quad (41)$$

The mean aerodynamic chord is not to be confused with the average wing chord, defined as

$$c_{avg} = \frac{S}{b} \quad (42)$$

The lift on an individual wing half may be thought of as acting at a distance

$$y_s = \frac{2}{S} \int_0^s c(y) dy \quad (43)$$

from the plane of symmetry.

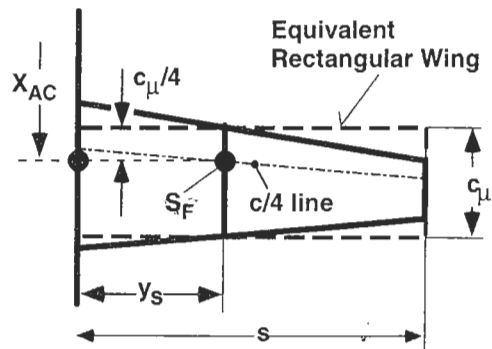


Fig. 42: Mean aerodynamic chord and equivalent rectangular wing.

c_{μ}	mean aerodynamic chord
X_{AC}	location of wing aerodynamic center
S_F	center of mass of $c/4$ -line, assuming local mass loading proportional to local chord
s	wing semi-span

Airfoil Geometry and Aerodynamic Characteristics

Airfoil families and profile catalogs

The aerodynamic properties of an airfoil are functions of its geometry, angle of attack, Reynolds number, and surface quality. The large number of geometric parameters allows the definition of a virtually unlimited variety of airfoil shapes. Designers are often faced with the difficult task of selecting airfoils based on various operational requirements, and it is therefore useful to classify airfoils systematically according to certain characteristics. A number of *airfoil families* have been defined and their geometric and aerodynamic data tabulated in airfoil catalogs.

Over the years, several profile series have been of particular significance to sailplane designers. A few of these are now of only historical importance. After the cambered flat plate used by Lilienthal in his first glider, the first family of airfoils were the Joukowski airfoils, defined and analyzed in closed form using conformal mapping. The Joukowski airfoils are more of theoretical interest rather than practical significance. Relatively few were suitable for use in actual aircraft. The Göttingen series followed, of which the Gö 535 and Gö 549 were frequently used in early sailplanes.

The NACA four- and five-digit profile series are classified according to the parameters defining their geometry. Although seldom used in sailplanes, they find occasional application even today in powered aircraft. The NACA 6-series profiles are *laminar profiles*, designed specifically to allow the boundary layer to remain laminar over the forward part (30-60% chord) of the airfoil. These airfoils were quite well suited to the needs of sailplanes and found frequent application in early high-performance sailplanes. Experimental and theoretical aerodynamic data for these NACA profile series are found in a report by I. H. Abbott and A. E. von Doenhoff [1]. See also F. W. Riegels [191]. One of the earliest design methodologies for laminar flow airfoils was developed by W. Pfenninger [99].

Airfoils specifically intended for sailplanes were developed by R. Eppler [174, 175, 178-180] and F. X. Wortmann [163, 168, 196, 198-202]. These airfoils led to tremendous improvements in sailplane performance and quickly replaced virtually all earlier profiles. A large body of experimental data for these airfoils was obtained in the Stuttgart laminar wind tunnel [203] and published in the well-known Stuttgart Profile Catalog [168]. See

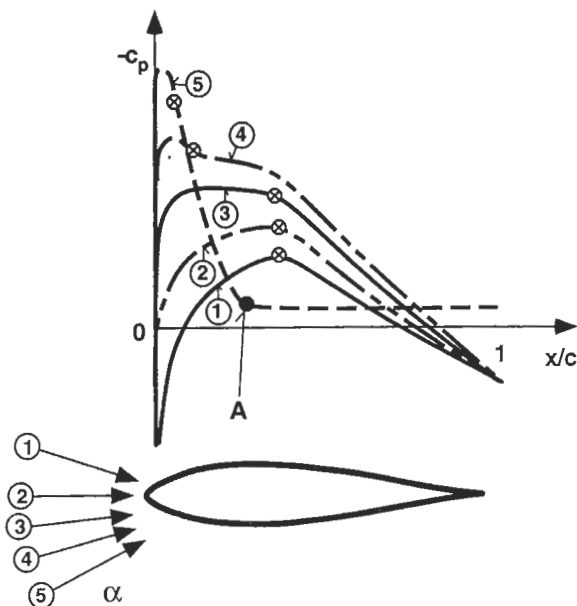


Fig. 43: Pressure distribution over a symmetrical airfoil at various angles of attack.

- ① - ⑤ upper surface pressure distribution at various angles of attack (see also Fig. 44)
- ② zero angle of attack, upper and lower surface pressure distribution
- ⊗ boundary-layer transition point
- A separation point

also [164, 167].

Further laminar airfoils were developed by K. H. Horstmann and A. Quast [182, 193] at the German Aerospace Center (DLR, formerly DFVLR). The drag of these airfoils is minimized by inhibiting the formation of laminar separation bubbles either by use of pneumatic turbulators or application of a special flow-tripping "zig-zag" tape [72, 74, 170] or "bump tape" [165, 166, 183-185]. More recently, L. M. M. Boermans and his students at the Delft University of Technology have developed and tested several very low drag airfoils [74, 170-172]. Delft's low-turbulence wind tunnel proved a valuable asset in this research. Additional work by D. M. Somers and M. D. Maughmer in the USA include a profile specially developed for the World Class [169, 188, 195].

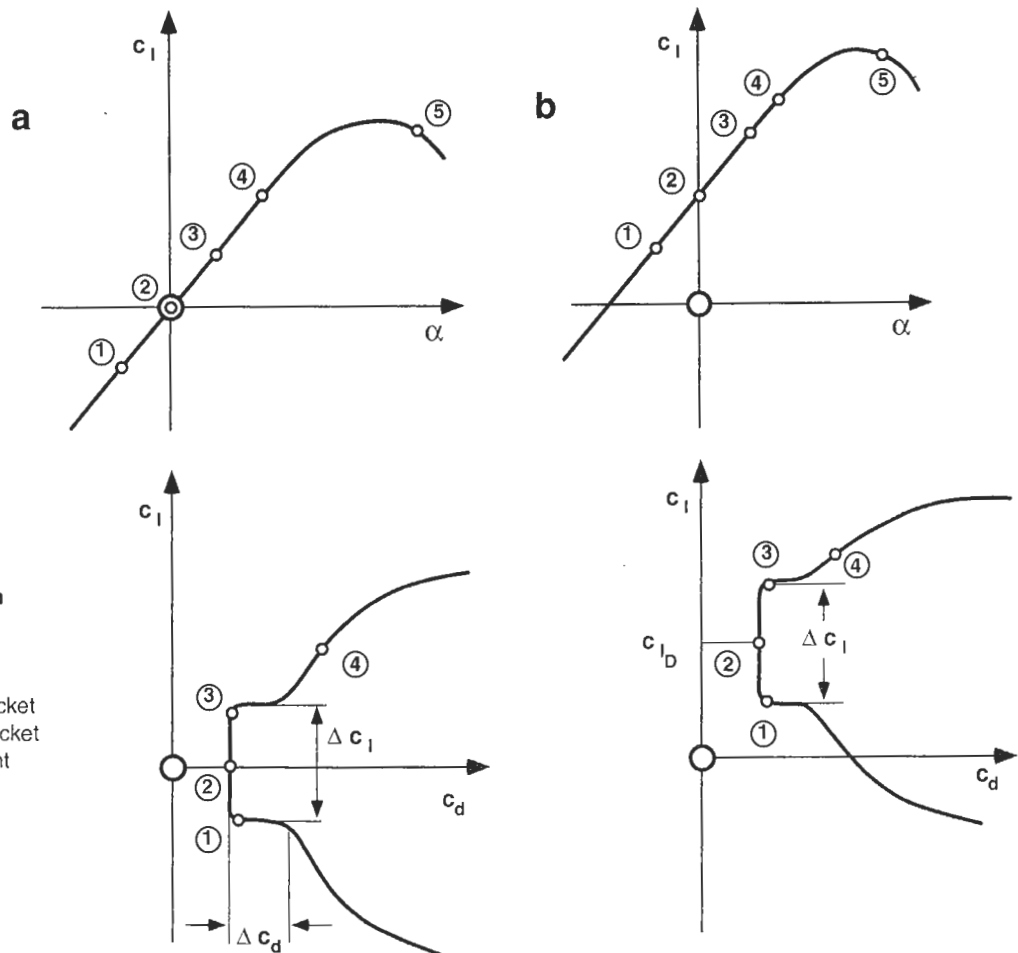


Fig. 44: Laminar bucket in airfoil polar.

- a) symmetric airfoil
- b) cambered airfoil
- Δc_l width of laminar bucket
- Δc_d depth of laminar bucket
- c_{l_0} design lift coefficient

The laminar bucket

The boundary layer on an airfoil operating at typical sailplane Reynolds numbers remains laminar until slightly beyond the point of minimum static pressure. For small angles of attack, this minimum pressure point occurs near the location of maximum thickness. For this reason, laminar airfoils are characterized by a relatively aft location of the point of maximum thickness.

However, the pressure distribution also varies with the angle of attack. This may be examined in detail taking a symmetrical airfoil as an example. At $\alpha = 0$, a symmetrical airfoil generates identical pressure distributions over the upper and lower surface. If an angle of attack is introduced,

additional pressure variations are superimposed on these basic $\alpha = 0$ distributions. The resultant force of this modified pressure distribution appears as lift at the 1/4-chord (aerodynamic center). This is related to the pressure distribution by observing that the pressure differential over the forward portion of the airfoil increases much more rapidly with angle of attack than the pressure differential on the aft portion of the airfoil. This distortion of the basic $\alpha = 0$ pressure distribution has an effect on the location of the point of minimum pressure and, in turn, the boundary-layer transition point.

This is made clearer by considering the effects of successive increases in angle of attack (Fig. 43). We consider only the upper surface as this is where the greatest pres-

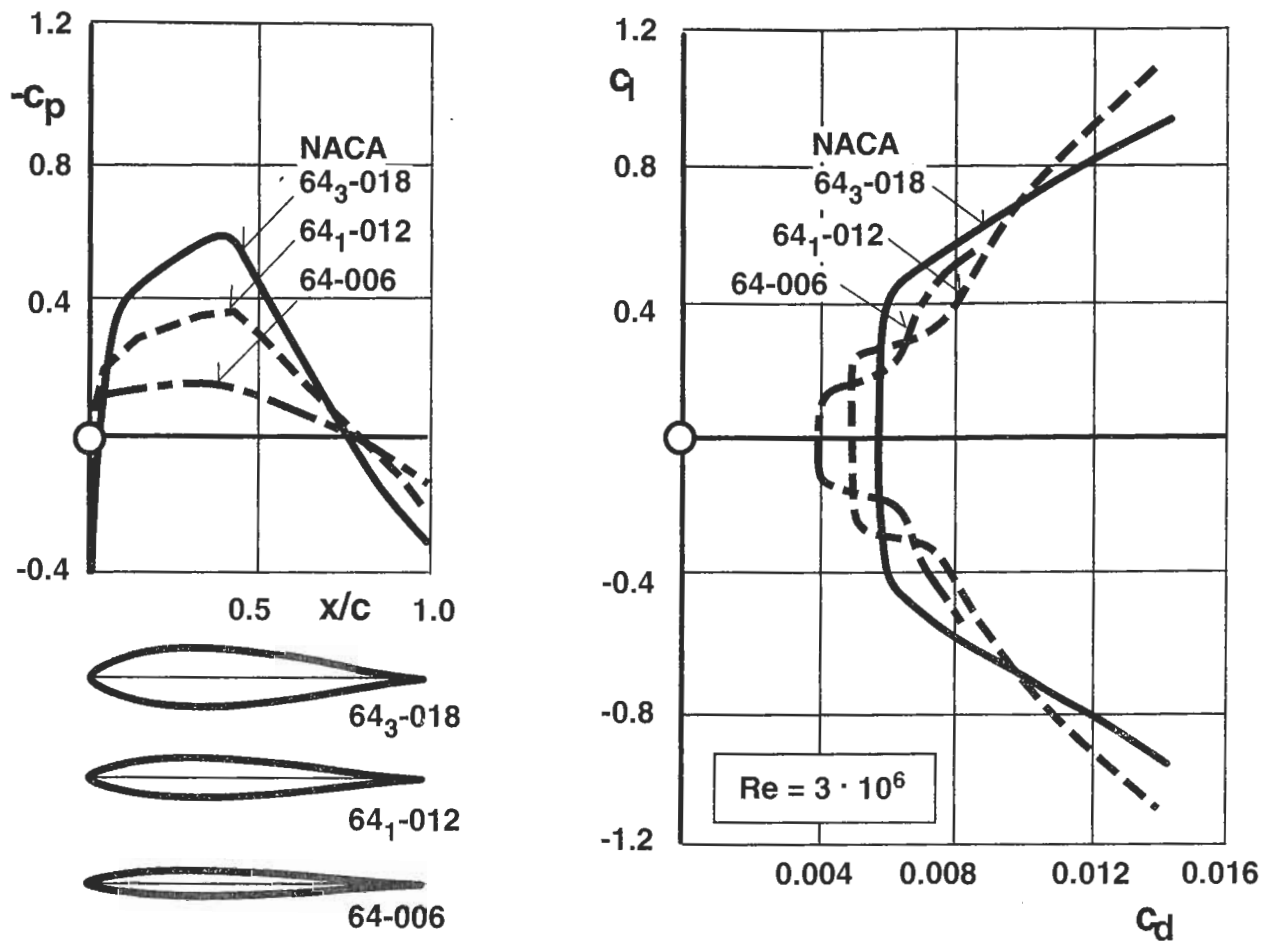


Fig. 45: Effect of airfoil thickness on pressure distribution and drag polar (from [1]).

sure variations due to angle of attack are expected. At negative angles of attack it is the lower surface that becomes critical.

Figure 43 shows the airfoil pressure distribution for four successively higher angles of attack. At small angles of attack the location of minimum pressure (and thus the boundary-layer transition point) is located relatively far aft on the airfoil. As the angle of attack is increased beyond a certain value, the minimum pressure and boundary-layer transition points shift relatively abruptly toward the airfoil leading edge. The portion of the boundary layer that remains laminar is shortened considerably, with a corre-

sponding increase in drag. If the angle of attack is further increased, the pressure gradient becomes so steep that the flow separates, with a further increase in drag as well as a decrease in lift.

Both flow separation and the migration of the boundary-layer transition point are easily recognized in the airfoil drag polars (Fig. 44). While the drag at small angles of attack may be quite low, beyond a certain angle of attack a rapid increase may be observed due to the forward shift in the boundary-layer transition point. The region of reduced drag at low angles of attack is the *laminar drag bucket*. The width of the laminar bucket defines the c_l range over which

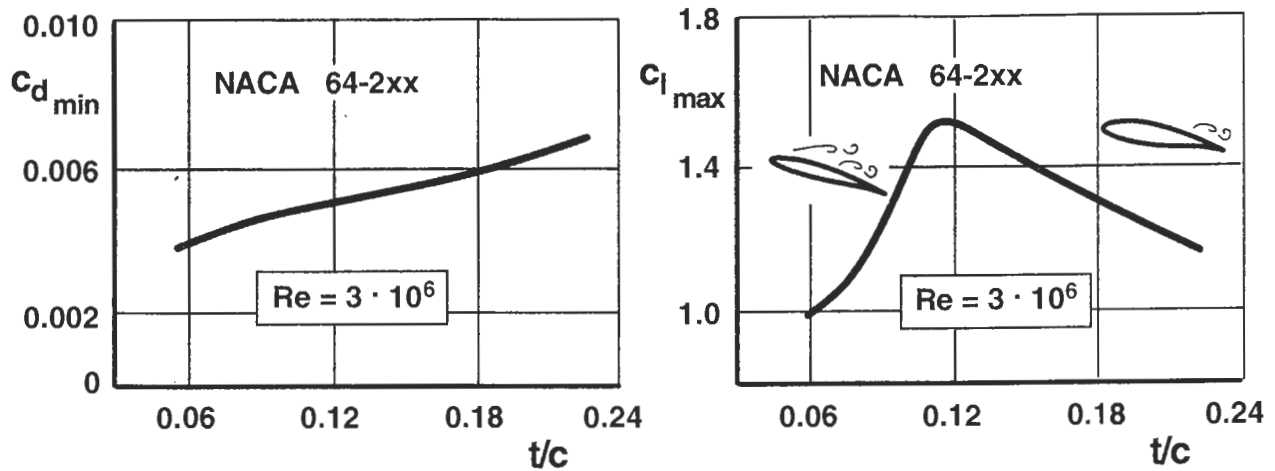


Fig. 46: Influence of airfoil thickness on minimum drag and maximum lift coefficient (from [1]).

reduced drag is present, and its depth is the drag reduction itself. Boundary-layer separation at high angles of attack occurs outside the laminar bucket and is recognizable as an additional increase in drag.

The same considerations apply to cambered airfoils. Here, however, the camber of the mean line generates an additional pressure variation that is superimposed over the basic pressure distribution. The laminar bucket shifts upward (that is, towards higher values c_l — Fig. 44). The value of c_l lying in the center of the laminar bucket is the *design lift coefficient*.

Influence of airfoil geometry

Airfoil selection is critical to sailplane design, and proper airfoil selection in turn necessitates a fundamental understanding of the effects of individual airfoil geometric parameters. These effects are illustrated with the example of the NACA 6-series airfoils, at one time frequently used in high performance sailplanes.

The designation numbers of the 6-series airfoils contain some useful information regarding their aerodynamic characteristics. Take for example the NACA 65₂-415. The first digit denotes the 6-series. The next digit indicates the location (in tenths of a chord) of the lowest static pressure for the basic symmetrical section at zero lift (5 → $x_d = 0.50c$).

This is usually near the point of maximum airfoil thickness. The subscript is half the width of the laminar bucket (2 → $\Delta c_l = 0.4$). The first digit following the hyphen defines the design lift coefficient (4 → $C_{l_d} = 0.4$) and the final two digits provide the airfoil thickness (15 → $d = 0.15c$). This numbering scheme allows the effects of various airfoil design parameters to be examined using data from airfoil catalogs such as [1].

The effects of varying the airfoil thickness are most apparent in a symmetrical airfoil. The upper and lower surface pressure distributions on a symmetrical airfoil at zero angle of attack are identical. If the thickness is varied while holding the basic form constant, the pressure distribution varies in proportion to the thickness (Fig. 45). The location of the point of minimum pressure remains unchanged. The most important effect of varying the thickness is observed in the drag polar. Thick airfoils exhibit relatively wide, shallow laminar drag buckets. As the airfoil is made thinner, the minimum drag coefficient is reduced, while the range of c_l for reduced drag — that is, the laminar drag bucket — becomes narrower.

Figure 46 shows the variation in minimum drag and maximum lift coefficient directly as a function of airfoil thickness. Steep pressure gradients observed over the aft portions of the thicker airfoils increase the likelihood of boundary-layer separation, particularly at high angles of attack. This is why the maximum lift coefficient diminishes with increas-

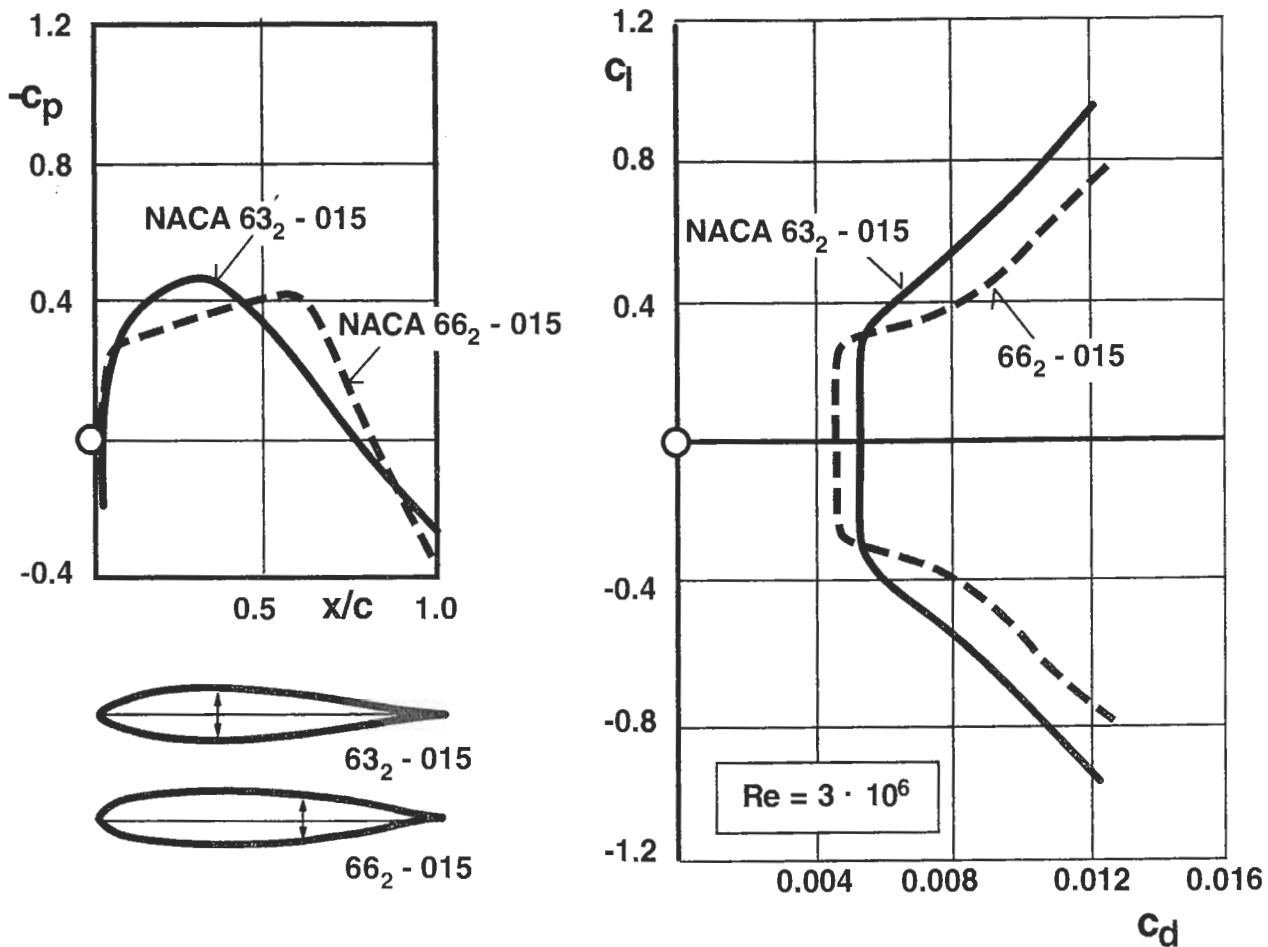


Fig. 47: Effect of location of point of maximum thickness on airfoil performance (from [1]).

ing airfoil thickness (Fig. 46). Below around 12% thickness the maximum lift coefficient also decreases since the leading edge becomes sharper and the flow tends to separate at this location. From a practical point of view, this phenomenon places a lower limit on the thickness of airfoils used in horizontal and vertical stabilizers.

As discussed, the chordwise location of the point of maximum thickness determines the location of the minimum static pressure, and in turn influences the boundary-layer transition point (Fig. 47). Typically, the point of maximum thickness lies between 30% and 50% of the airfoil chord (NACA 63, 64, and 65-series). If the point of maximum

thickness is shifted further aft (as with, for example, the NACA 66-series), the adverse pressure gradient in the aft portion of the airfoil becomes too steep, leading to premature separation.

Although the position of maximum thickness has little influence on the width of the laminar bucket, it has a considerable effect on its depth. Shifting the position of maximum thickness aft may however have a detrimental effect outside the laminar bucket due to increased adverse pressure gradients and flow separation.

If the airfoil is cambered, the resulting asymmetry gives rise to differences in pressure distribution over the upper

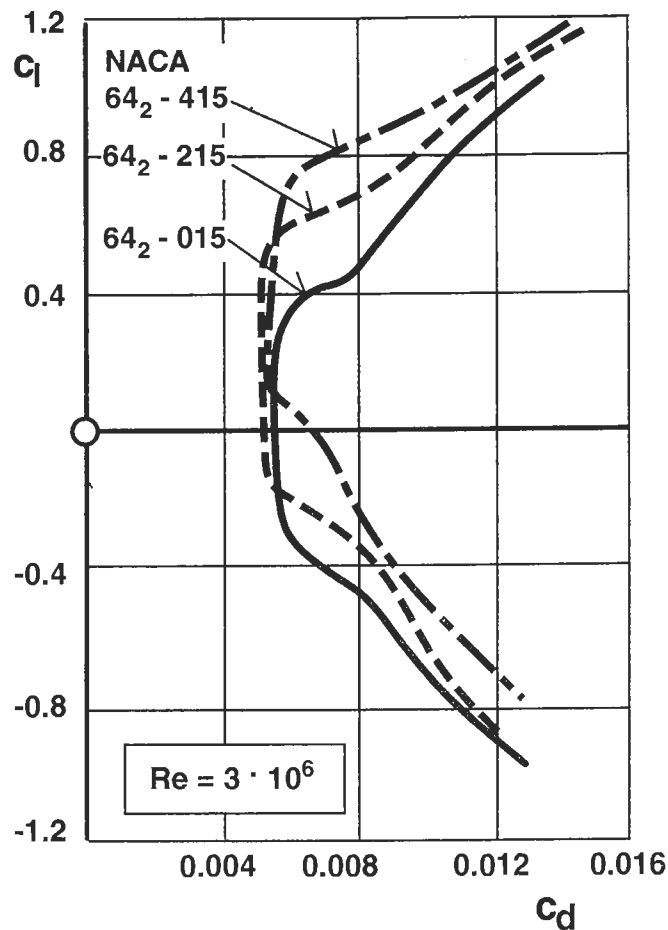
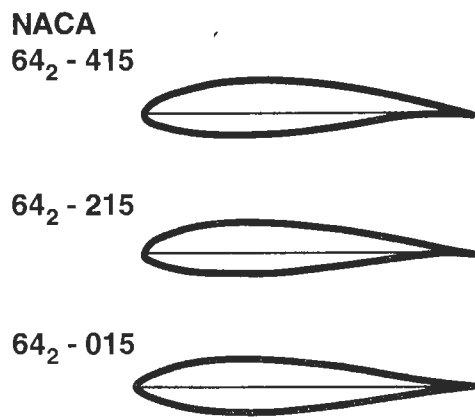


Fig. 48: Effect of camber on drag polar [1].

and lower surface, even at zero angle of attack. On the upper surface, the pressure shifts upward (in the $-c_p$ direction) and on the lower surface, downward (in the $+c_p$ direction). The effect is proportional to the maximum camber. Camber is usually introduced in the NACA 6-series airfoils using a mean line that produces a uniform increase in velocity distribution on the upper surface and a uniform decrease on the lower surface (the "a = 1.0" mean line). The velocity gradients, which are of primary importance to the development of the boundary layer, do not change. Consequently, although the center of the drag bucket shifts to a new design lift coefficient, the width and depth of the bucket remain essentially unchanged (Fig. 48). As the maximum camber increases, the laminar bucket shifts in

the direction of increased lift coefficient. Unlike the airfoil thickness and position of maximum thickness, the degree of camber and the chordwise position of maximum camber have a very strong influence on the pitching moment. Figure 49 shows an example of the increase in zero-lift angle, zero-lift moment, and maximum lift coefficient with increasing camber.

As the name suggests, a camber-changing flap has an effect similar to that of airfoil camber (Fig. 49). Camber-changing flaps allow the aerodynamic characteristics of the airfoil to be changed in flight. Specifically, the laminar bucket may be shifted as required by repositioning the flaps. Since camber-changing flaps introduce camber at a relatively aft location on the airfoil, they have an especially

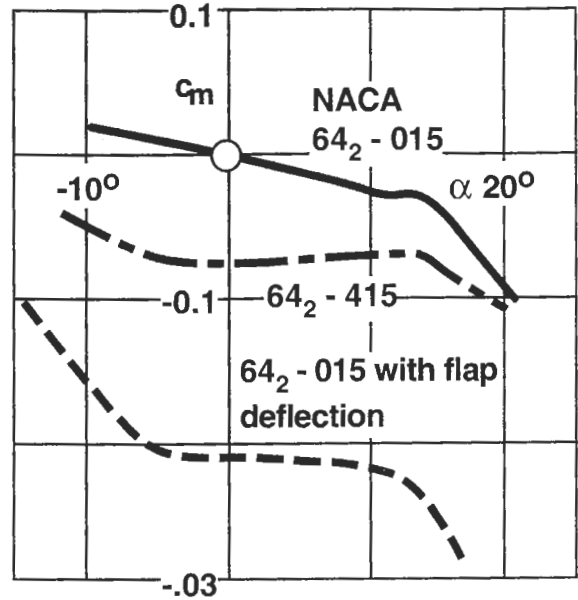
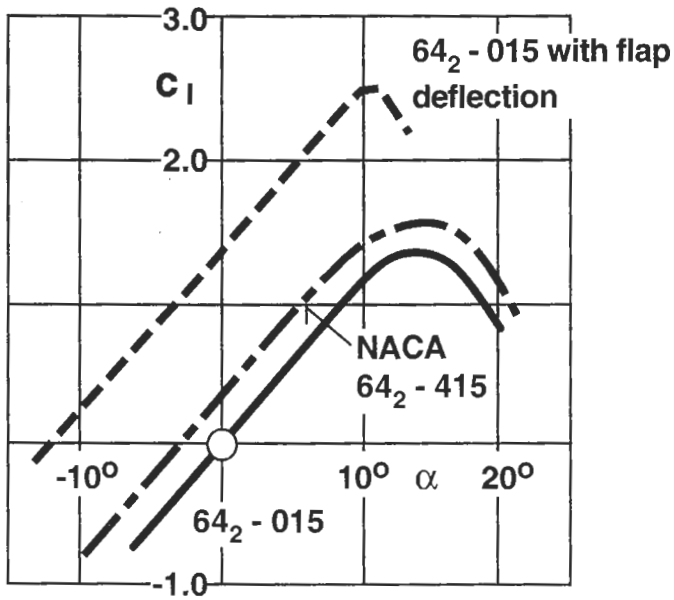


Fig. 49: Influence of camber and flap deflection on lift and pitching moment characteristics.

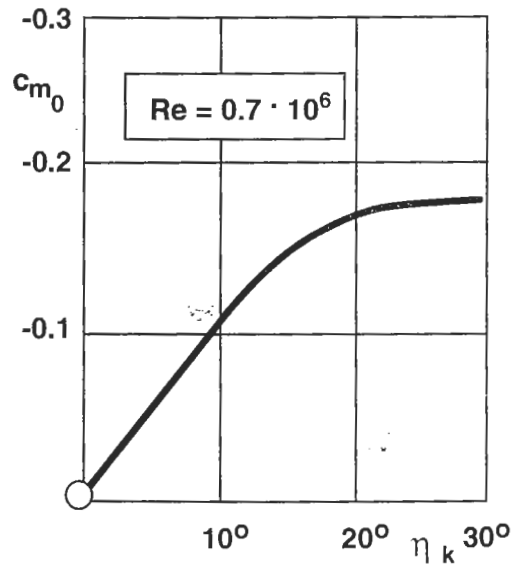
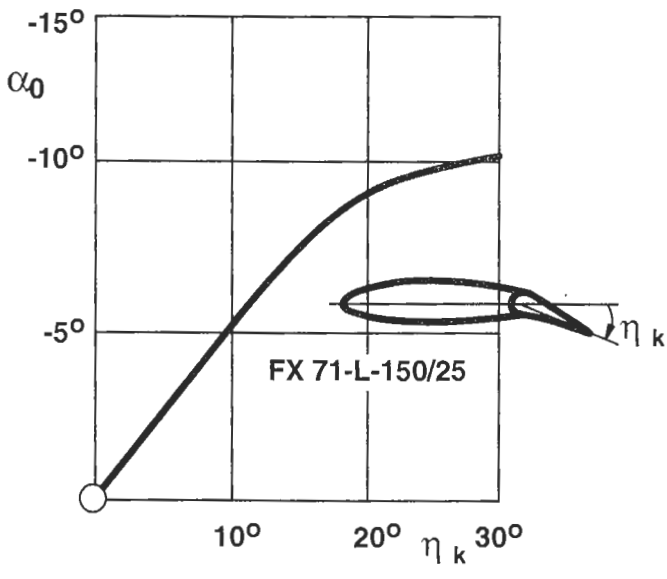


Fig. 50: Influence of flap deflection on zero-lift angle and zero-lift pitching moment.

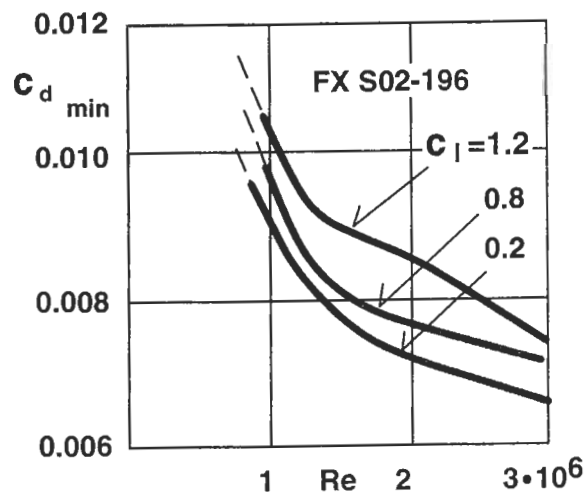
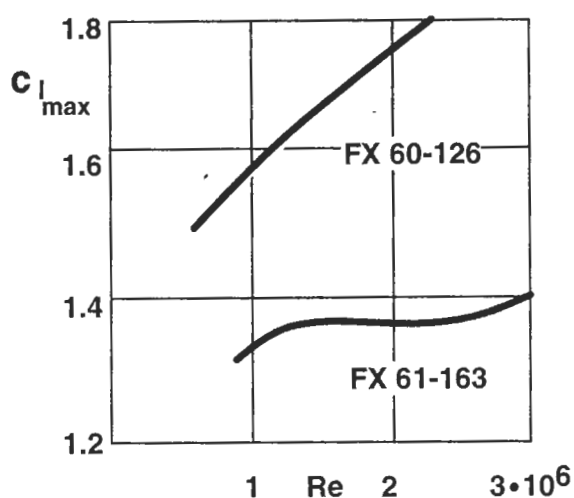


Fig. 51: Variation of maximum lift coefficient and minimum drag with Reynolds number.

strong effect on the zero-lift pitching moment (Fig. 50).

Reynolds number and surface quality

As discussed, Reynolds number and surface quality have a considerable effect on the development of the boundary layer. In practical terms, the effects are seen mainly in the lift-curve slope, minimum drag, and maximum lift coefficient. At Reynolds numbers typical of sailplanes, airfoil performance generally diminishes with decreasing Reynolds number. In particular, the increased tendency to form laminar separation bubbles and the overall increase in viscous losses leads to a reduction in the lift curve slope, the maximum lift coefficient, and an increase in minimum drag (Fig. 51).

The influence of surface quality is of particular interest in view of the high likelihood of insect impact during flight as well as the possibility of operating in rain [171, 197, 235]. In both cases the boundary layer becomes turbulent near the airfoil leading edge. In turn, the minimum drag coefficient increases, depending on airfoil thickness, to a value ranging from 0.008 to 0.012. At higher lift coefficients, additional drag penalties arise due to flow separation near the trailing edge. An increase in surface roughness leads to greater energy losses in the boundary layer, leaving it less able to overcome the adverse pressure gradients and

remain attached in the aft portion of the airfoil.

Drag penalties due to insect contamination appear to be less severe for thin airfoils with sharp leading edges than for thick airfoils with large leading-edge radii.

Wing Planform and Lift Distribution

Elliptical wings

For the high aspect ratio wings typically found on sailplanes, the chordwise pressure distribution at each spanwise location depends only on the airfoil geometry at that location and the corresponding effective angle of attack. Planform and twist affect only the spanwise lift distribution. The lift distribution has an important effect on

- load assumptions for the structural analysis,
- induced drag,
- wing/fuselage and wing/empennage interference effects, and
- stall characteristics

A special case in wing theory is the untwisted elliptical planform wing. Prandtl's lifting-line theory predicts that this wing will generate an elliptical spanwise circulation and